Imaging the Subsurface Plumbing Complex of Steamboat Geyser and Cistern Spring with Hydrothermal Tremor Migration Using Seismic Interferometry

Sin-Mei Wu[1], Fan-Chi Lin[1], Jamie Farrell[1], William Keller[2], Erin B White[2], and Jefferson D G Hungerford[2]

[1]University of Utah
[2]Yellowstone Center for Resources

November 22, 2022

Abstract

Steamboat Geyser in Yellowstone National Park is the tallest active geyser on Earth and is believed to have hydrologic connection to Cistern Spring, a hydrothermal pool ~100 m southwest from the geyser vent. Despite broad scientific interest, rare episodic Steamboat eruptions have made it difficult to study its eruption dynamics and underground plumbing architecture. In response to the recent reactivation of Steamboat, which produced more than 115 eruptions since March 2018 already, we deployed a dense seismic nodal array surrounding the enigmatic geyser in summer 2019. The array recorded an abundant 1-5 Hz hydrothermal tremor originating from phase-transition events within both Steamboat and Cistern. To constrain the spatiotemporal distribution of the tremor sources, an interferometric-based polarization analysis was developed. The observed tremor locations indicate that the conduit beneath Steamboat is vertical and extends down to ~120 m depth and the plumbing of Cistern includes a shallow vertical conduit connecting with a deep, large, and laterally offset reservoir ~60 m southeast of the surface pool. No direct connection between Steamboat and Cistern plumbing structures is found. The temporal variation of the tremor combined with in situ temperature and water depth measurements of Cistern, do reveal the interaction between Steamboat and Cistern throughout the eruption/recharge cycles. The observed delayed responses of Cistern in reaction to Steamboat eruptions and recharges suggest the two plumbing structures might be connected through a fractured/porous medium instead of a direct open channel, consistent with our inferred plumbing structure.

1

1 **Imaging the Subsurface Plumbing Complex of Steamboat Geyser and Cistern Spring with**

2 **Hydrothermal Tremor Migration Using Seismic Interferometry**

3 **Sin-Mei Wu[1], Fan-Chi Lin[1,2], Jamie Farrell[1], William E. Keller[3], Erin B. White[3], and**

4 **Jefferson D.G. Hungerford[3]**

5

6 [1]Department of Geology and Geophysics, University of Utah, Salt Lake City, UT, USA

7 [2]Institute of Earth Sciences, Academia Sinica, Taipei, Taiwan

8 [3]National Park Service, Yellowstone Center for Resources, Yellowstone National Park, WY,

9 USA

10 Corresponding author: **Sin-Mei Wu (sinmei.wu@utah.edu)**

11

12 **Key Points:**

13 • We develop an interferometric-based polarization analysis to investigate high-resolution

14 spatiotemporal pattern of hydrothermal tremor.

15 • We construct the first image of the plumbing architecture for the Steamboat-Cistern

16 system to a depth of 140 m.

17 • We illuminate the recharge evolution of Steamboat Geyser and Cistern Spring and the

18 dynamic subsurface interaction between the two features.

19

20

21 **Abstract**

22 Steamboat Geyser in Yellowstone National Park is the tallest active geyser on Earth and is

23 believed to have hydrologic connection to Cistern Spring, a hydrothermal pool ~100 m

24 southwest from the geyser vent. Despite broad scientific interest, rare episodic Steamboat

25 eruptions have made it difficult to study its eruption dynamics and underground plumbing

26 architecture. In response to the recent reactivation of Steamboat, which produced more than 115

27 eruptions since March 2018 already, we deployed a dense seismic nodal array surrounding the

28 enigmatic geyser in summer 2019. The array recorded an abundant 1–5 Hz hydrothermal tremor

29 originating from phase-transition events within both Steamboat and Cistern. To constrain the

30 spatiotemporal distribution of the tremor sources, an interferometric-based polarization analysis

31 was developed. The observed tremor locations indicate that the conduit beneath Steamboat is

32 vertical and extends down to ~120 m depth and the plumbing of Cistern includes a shallow

33 vertical conduit connecting with a deep, large, and laterally offset reservoir ~60 m southeast of

34 the surface pool. No direct connection between Steamboat and Cistern plumbing structures is

35 found. The temporal variation of the tremor combined with in situ temperature and water depth

36 measurements of Cistern, do reveal the interaction between Steamboat and Cistern throughout

37 the eruption/recharge cycles. The observed delayed responses of Cistern in reaction to Steamboat

38 eruptions and recharges suggest the two plumbing structures might be connected through a

39 fractured/porous medium instead of a direct open channel, consistent with our inferred plumbing

40 structure.

41

1 Introduction

43 Steamboat Geyser in Yellowstone National Park is the tallest active geyser on Earth — recorded

44 eruption heights have exceeded 110 m since 1962 (White et al., 1988). In addition to the

45 fascinating water discharging phase lasting less than an hour after the onset of an eruption,

46 Steamboat earned its name from having the roaring steam phase that could create a steam

47 column hundreds-of-meters high above the ground and persist for days (White et al., 1988).

48 Steamboat's major eruptions are episodic with only three major active phases recorded: in the

49 1960s, 1980s, and the ongoing eruptions since March 2018. The current active phase has covered

50 more than 115 eruptions to date and has been hypothesized to be associated with shallow

51 magmatic volatile accumulation (Wicks et al., 2020). Sporadic eruptions did occur between

52 active phases but most of these eruptions were not directly witnessed and only were accounted

53 for after the fact. The recorded latest singular eruption before the current active phase was in

54 2015. Since 1966, Cistern Spring located 100 m southwest of Steamboat, was observed to have

55 its water level drop (by 5–7 m) and surface temperature decrease (about 20 degrees) after

56 Steamboat's major eruption (White et al., 1975), suggesting these two features are

57 interconnected. Such hydrologic connection persists in the current active phase, however, the

58 exact location where Steamboat and Cistern are physically connected and how the interaction of

59 the two might affect the eruption/recharge dynamics of Steamboat remain largely elusive.

60

61 The plumbing geometry of a geyser can be complex and exerts direct control over its eruption

62 and recharge dynamics (Hurwitz & Manga, 2017). Narrow constrictions make the supersonic

63 (choked) flow possible for eruptions, and the depth extent of the fluid pathway including the

64   reservoir location governs the vapor mass fraction in the system before an eruption, which is

65   indicative of exit velocity that controls the eruption height (Kieffer, 1989; Karlstrom et al., 2013;

66   Reed et al., 2019). Shallow reservoirs or cavities that allow the vapor and liquid two-phase

67   mixture to accumulate within are proposed to modulate a geyser's eruptive characteristics (i.e.,

68   preplay, minor and major eruptions) and may be responsible for the geyser's (ir)regularity

69   (Adelstein, et al., 2014; Belousov et al., 2013; Munoz-Saez et al., 2015a; Rudolph et al., 2018;

70   Vandemeulebrouck et al., 2014). Side channels and offset reservoirs/cavities have been

71   proposed/found in Old Faithful geyser (Hutchinson et al., 1997; Vandemeulebrouck et al., 2013;

72   Wu et al., 2017), Lone Star geyser (Vandemeulebrouck et al., 2014) in Yellowstone, Geyser

73   Valley in Russia (Belousov et al., 2013), Strokkur geyser in Iceland (Eibl et al., 2020), and El

74   Jefe in Chile (Ardid et al., 2019). Permeable medium that allows pressure transmission has been

75   inferred to govern the interaction between nearby hydrothermal features (e.g., El Tatio in Chile;

76   Munoz-Saez et al., 2015b).The conduits of natural geysers are irregular, contorted, and can

77   contain structures that are two orders of magnitude different in scale (e.g., centimeter choke

78   point versus meter wide cavity; Belousov et al., 2013; Hutchinson et al., 1997), which pose

79   significant challenging in geophysical imaging.

80

81   In situ physical probes such as temperature, pressure loggers, and video cameras have been used

82   to depict the direct portrayal and physical condition of the shallow conduit (Belousov et al.,

83   2013; Hutchinson et al., 1997; Munoz-Saez et al., 2015a, 2015b; White et al., 1988; Walter et al.,

84   2018). However, the depth extent of such measurements have been hampered by constrictions

85   and lateral turns thereby limiting them to ~25 m depth at most. Ground penetrating radar is able

86   to image high-resolution spatiotemporal fluid distribution but is also restricted to mapping only

87   the shallowest part of the system (e.g., <5 m for Old Faithful; Lynne et al., 2018). Resistivity

88   studies from electromagnetic surveys are widely applied for geothermal exploration but the fine-

89   scale study of a hydrothermal system's plumbing has been less common (e.g., Carr et al., 2019).

90

91   Early seismic studies mainly focused on understanding the source origin of the hydrothermal

92   tremor (e.g., bubble collapse and nucleation) and their relation to a geyser's recharge/eruption

93   dynamics (Kieffer, 1984, 1989; Kedar et al., 1996, 1998; Rinehart, 1965). During recharge,

94   bubbles form or collapse in response to changes in temperature and hydrostatic pressure within

95   the water column, which progressively brings heat from deep to shallow as the less-dense

96   bubbles rise driven by buoyancy (Vandemeulebrouck et al., 2014; Wu et al., 2019). When the

97   entire column is close to the saturation temperature, small but sufficient pressure perturbations

98   from the surficial preplay activity reduce the hydrostatic pressure and give rise to boiling in the

99   deep conduit by lowering the boiling temperature, thus an eruption can occur (Kieffer, 1989).

100

101   With the recent availability of multiple instruments and array data, subsurface hydrothermal

102   structures such as major reservoirs and the local geologic deposits can now be inferred using

103   both active source (Ardid et al., 2019; Caylor, 2020; Price et al., 2015) and passive (Wu et al.,

104   2017) seismic imaging methods. Spatiotemporal patterns of the source locations of hydrothermal

105   tremor can be further used to illuminate high-resolution plumbing geometry and the

106   recharge/eruption dynamics. For example, shallow and laterally shifted reservoirs are proposed

107   based on the ground deformation (using long-period seismic data) induced from subsurface

108   offset pressure sources at El Jefe in Chile (Ardid et al., 2019), and based on the locations of high-

109   frequency tremor (>10 Hz) at Old Faithful and at Lone Star geysers in Yellowstone

110   (Vandemeulebrouck et al., 2013, 2014). Temporal changes in resonance frequency of the tremor

111   also reveal the fluid oscillatory behavior between the conduit and the offset reservoir

112   (Vandemeulebrouck et al., 2013; Rudolph and Sohn, 2017; Rudolph et al., 2018). While the

113   high-frequency tremor energy is predominant in seismic records, the weak low-frequency tremor

114   (1–5 Hz) was initially discovered at Old Faithful geyser where it solely provided insight into the

115   deep plumbing system (20–80 m depth) and illustrated the full recharge evolution from the 4D

116   view of the tremor (Wu et al., 2019).

117

118   In this study, following our earlier study of Old Faithful (Wu et al., 2019), we investigate the

119   plumbing architecture of the Steamboat/Cistern system by imaging the hydrothermal tremor

120   source migration. In particular, in response to the recent rejuvenation of Steamboat, we deployed

121   two temporary dense seismic arrays; one in May–June 2018 and one in June–July 2019 to record

122   the active eruptions. The 2019 data, which will be the focus of this study, covers six eruption

123   cycles and has a larger array aperture compared to the 2018 array. In section 2, we introduce the

124   array design and identify distinct 1–5 Hz tremor excited by Steamboat and Cistern; in section 3,

125   we describe the interferometric-based method that we develop to simultaneously locate the

126   tremor in both space and time; in section 4, we summarize the observed 4D pattern of the tremor

127   and the plumbing architecture of both features; and in section 5, we discuss the implications of

128   the recharge/eruption dynamics and plumbing connection based on the seismic results and in situ

129   observations.

130

131   **2 Data**

132   **2.1 Seismic Nodal Array and In Situ Transducers**

133   In collaboration with the National Park Service (NPS) at Yellowstone, we deployed a seismic

134   nodal array in the vicinity of Steamboat Geyser and Cistern Spring between 13 June and 22 July

135   2019 (Figure 1a). The array was composed of 50 three-component 5-Hz geophones with a 1000

136   Hz sampling rate. The array aperture was ~250 m and the station spacing was about 15–35 m.

137   During the experiment, a total of seven Steamboat major eruptions occurred with six intervals

138   varying between 3 and 8 days (Figure 1b). Because the analyses in this study are based on

139   seismic interferometry and all the geophones use the same type of instrument, we did not

140   removed the instrument response. In addition to seismic recording, the NPS placed pressure and

141   temperature transducers in Cistern Pool located at ~3.5 m depth between 11 July and 18 July

142   2019. Both in situ measurements were recorded at 1 minute intervals. The continuous recordings

143   are used to monitor the physical and thermal status of Cistern pool during the Steamboat eruption
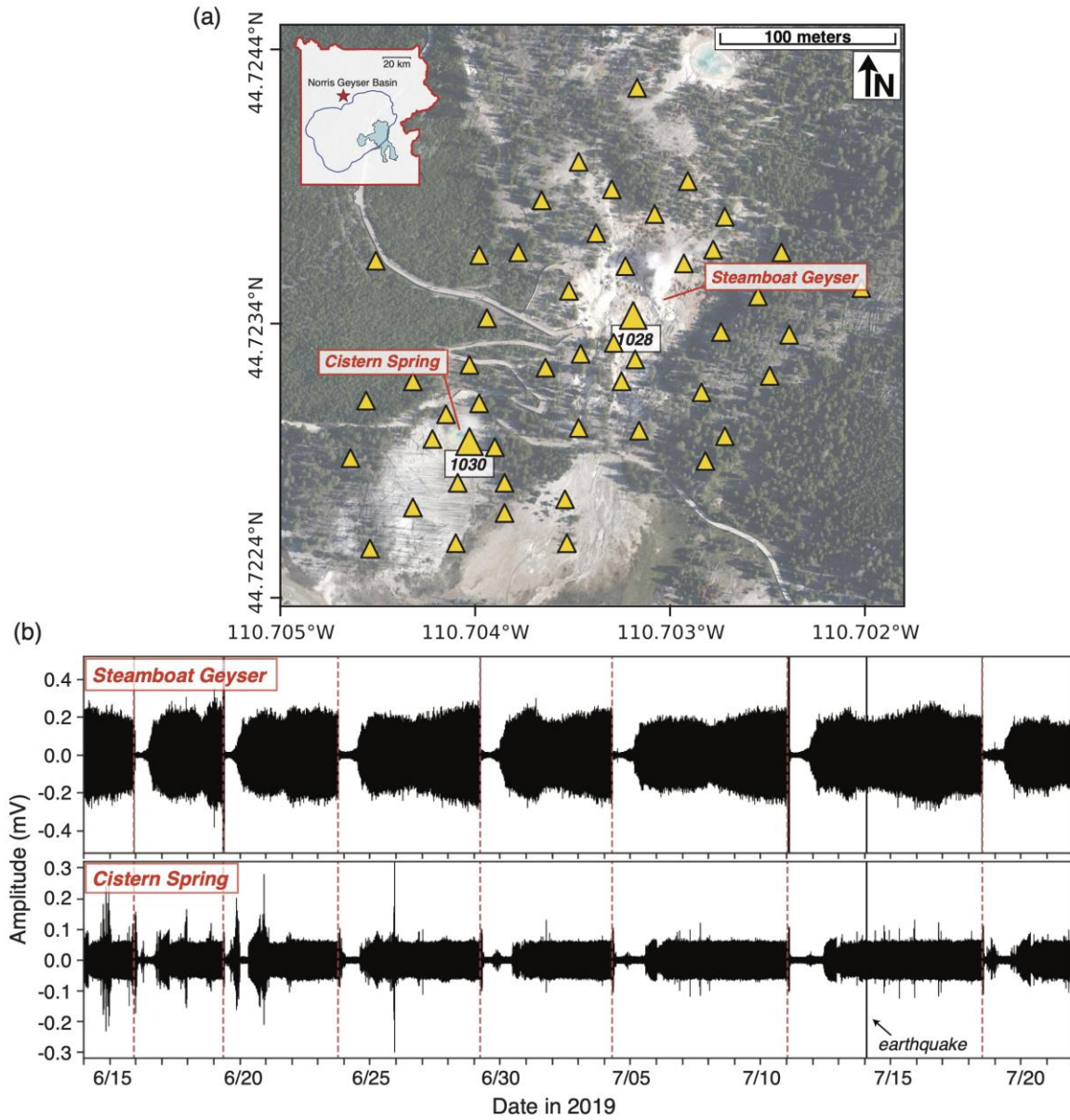
144   cycle.

145

146

Figure 1. (a) The seismic nodal array deployed between 13 June and 22 July 2019. The yellow triangles represent the station location. The red star in upper-left inset denotes the location of Norris Geyser Basin where Steamboat is located within the Yellowstone National Park (red boundary). The blue line in the inset delineates the boundary of the 0.64-Ma caldera. (b) The month-long, 1–5 Hz seismic energy associated with steam-liquid phase transition emitted from Steamboat Geyser (station 1028) and Cistern Spring (station 1030). The red-dashed lines mark the Steamboat eruption times obtained from GeyserTimes (2020). The unit of the seismogram is millivolt.

155

156

157   **2.2 Distinct Hydrothermal Tremor from Steamboat and Cistern**

158   From the seismographs recorded by the nearest stations, we observe clear cyclic low-frequency

159   (1–5 Hz) seismic energy, hereafter tremor, emitted from both Steamboat and Cistern (Figure 1b).

160   The tremor amplitudes are higher prior to Steamboat's major eruptions and drop sharply

161   afterward, which highly resembles the temporal variation of the 1–5 Hz tremors observed at Old

162   Faithful Geyser (Wu et al., 2019). Different from the Old Faithful tremor, which intensified

163   monotonically before each eruption, the amplitude variations of Steamboat and Cistern tremor

164   are more variable and the tremor variation is distinct between the two features. This indicates

165   that the recharge process is more complicated for the Steamboat/Cistern system, possibly due to

166   its intertwined plumbing structure. To study the architecture and the dynamics of Steamboat and

167   Cistern, we explore the spatiotemporal pattern of the tremor origins below.

168

169   **3 Methods**

170   The distinct temporal patterns of tremor between Steamboat and Cistern demonstrate a

171   multisource environment within the seismic array. Traditional source locating methods relying

172   on arrival peaks and/or accurate velocity models (e.g., Gomberg et al., 1990; Guo et al., 2017;

173   Kao & Shan, 2004; Richards et al., 2006) does not work for the observed hydrothermal tremor as

174   no isolated event with discernable arrival was observed and the shallow velocity structure is

175   largely unknown. Moreover, as Steamboat and Cistern are only 100 m away, wavefield

176   interference likely occurred persistently across the entire array. To probe the spatiotemporal

177   pattern of the tremor, in this study, we further develop an interferometry-based polarization

178   analysis (Wu et al., 2019) to image the multi-source migration of the Steamboat/Cistern tremor.

179   The main workflow of the method is summarized in Figure 2 where the detailed description of

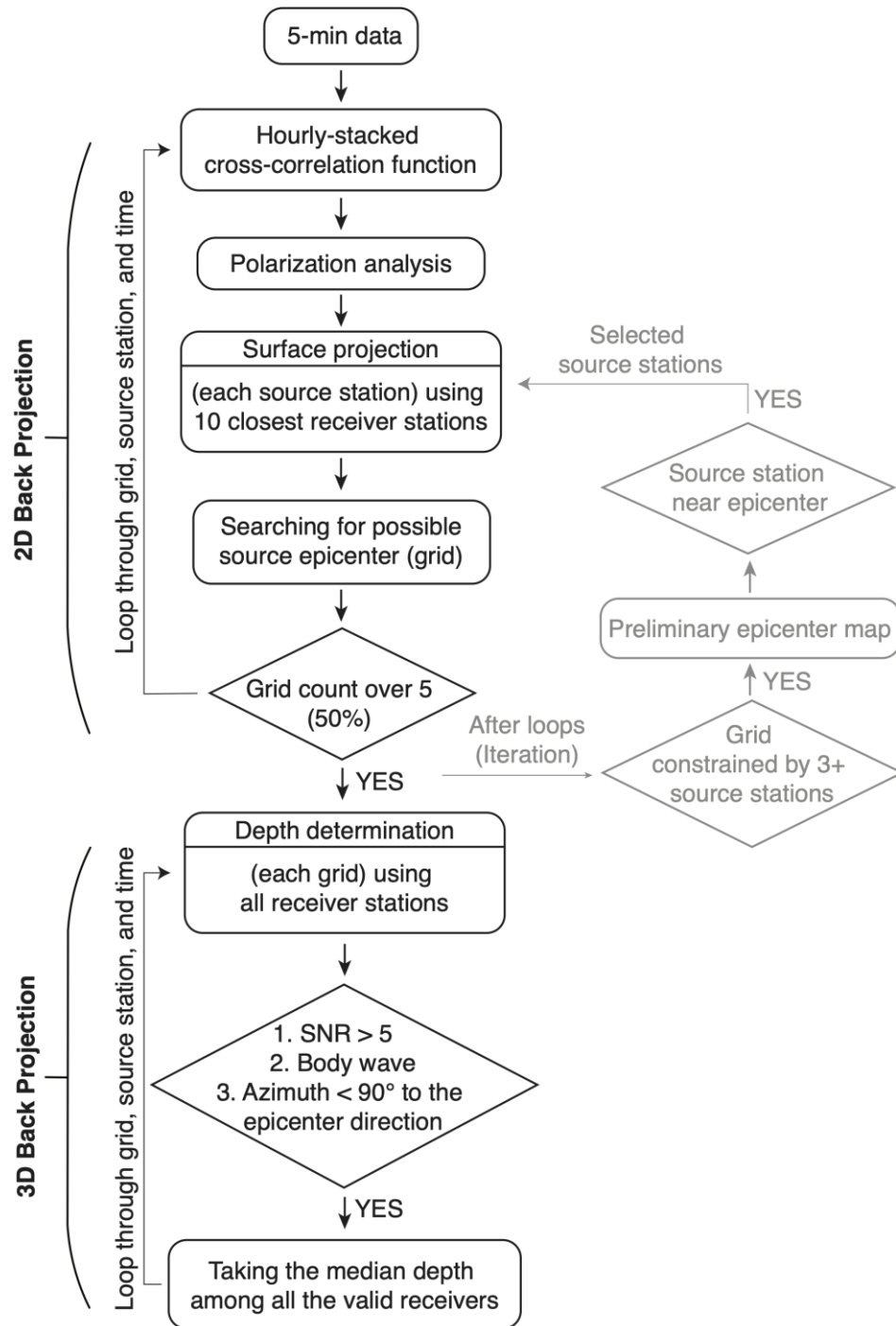180   each step is described in the following sections.

181

182 Figure 2. The workflow for the analyses in this study. The procedures in gray color are
183 for source station selection and can be iterated multiple times. In this study, we perform
184 two iterations to determine the virtual source station for each epicenter location.
185

186

187 **3.1 Seismic Interferometry**

188 To enhance and isolate the 1–5 Hz tremor signals emitted within the Steamboat/Cistern system,

189 we perform a multicomponent cross-correlation. The cross-correlation method has the advantage

190 of amplifying coherent signals observed at the two stations where signals at different lag times

191 represent signals originated from different source locations. The method is particularly effective

192 when a station is located close to a persistent tremor source. In such a case, the cross-correlation

193 wavefield constructed using that station as the common station (or source station) and all other

194 stations as receivers closely resemble the wavefield emitted by the tremor source but with a

195 spontaneous excitation (Wu et al., 2017, 2019). Moreover, for each receiver, by preserving the

196 relative amplitude between different components, the particle motion and hence the polarization

197 of the emitted wavefield can also be extracted using the three-component cross-correlation

198 functions (CCFs; Lin et al., 2014; Wu et al., 2019). We note that the main focus of this study is

199 to utilize the CCFs to investigate the tremor source property. This is different from the common

200 noise interferometry studies, which often focus on investigating wave propagation and

201 subsurface velocity structure (e.g., Shapiro et al., 2005).

202

203 Adapting the process we implemented on Old Faithful Geyser (Wu et al., 2019), we first

204 calculate the CCFs using 5-min nonoverlapping time windows, then perform temporal stacking

205 to obtain one-hour CCFs. For each 5-min window, we cross-correlate the vertical component

206 seismogram (Z) at a source station with all three-component seismograms (Z, E, and N) across

207   the entire array. Thus, the CCFs are expressed as ZZ, ZE, and ZN or ZZ, ZR, and ZT after

208   rotating to the radial (R) and transverse (T) directions. The relative amplitude information is

209   preserved by applying the identical spectral and temporal normalizations to all components from

210   the same time window (Bowden et al., 2015). For spectral normalization, we whiten the CCF

211   spectrums by the 90th percentile averaged three-component spectrum across the entire array. For

212   the temporal normalization, we first applied a Butterworth filter between 1 and 5 Hz to remove

213   high-frequency energy; then, all the filtered CCFs are normalized by the 90th percentile

214   maximum amplitude of the vertical-vertical CCFs across the entire array. Note that the

215   normalization process applied here is done one at a time for each source station. To obtain

216   nonoverlapping one-hour CCFs, we linearly stacked the normalized 5-min CCFs. Here, we

217   reference the one-hour CCFs based on the beginning time of each one-hour window.

218

219   Taking the station closest to Steamboat as the source, the CCFs 11 hours before an eruption

220   show a clear vertical-radial linear motion, indicative of a P wave, when the receiver is close (<40

221   m; Figure 3a). The wavefield converts to elliptical Rayleigh wave particle motions for distant

222   receivers (>60 m; Figure 3c) while a hybrid motion is observed in the intermediate distance (~50

223   m; Figure 3b). For the source station closest to Cistern, the CCFs also have clear P wave motion

224   in the vicinity of Cistern (Figure 3f). For receivers close to Steamboat, the presumed Cistern

225   tremor signals however are overwhelmed and interfered with the Steamboat signals, as the

226   dominant arrivals of CCFs lie within the negative lag time (Figures 3g and 3h). This indicates the

227   steamboat tremor is in general stronger compared to the Cistern tremor. In sections 3.2 and 3.3,

228   we will discuss how we only select the receivers close to the source station to investigate the

229   tremor source location. To automatically identify and characterize all tremor sources within the

230   Steamboat/Cistern system, in our following analyses, we consider all stations across our array as

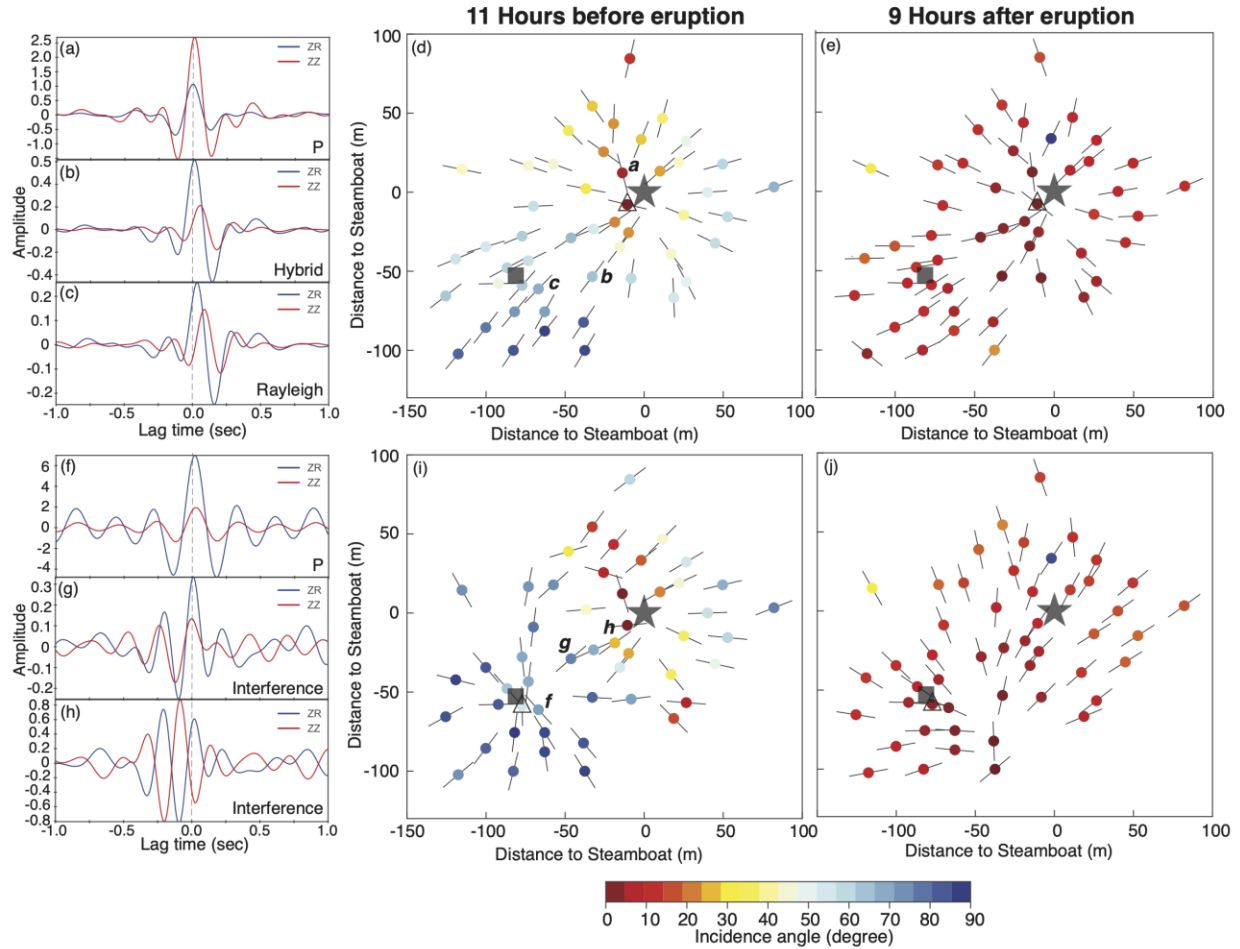231   possible source stations in addition to the stations that are closest to Steamboat and Cistern.

232

233   Figure 3. (a–c) Examples of vertical-vertical (ZZ) and vertical-radial (ZR) cross-
234   correlations between a common source station (the open triangle denoted in d) and
235   three different receiver stations (letters denoted in d). (d–e) Polarizations (bar: back
236   azimuth direction; color: incidence angle) of multi-component cross-correlations with a
237   common source station (open triangle) near Steamboat 11 hours before (d) and 9 hours
238   after (e) a major eruption. The black star and the black square denote Steamboat and
239   Cistern location, respectively. (f–h) Same as a–c but for a different common source
240   station and three different example receiver stations. (i–j) Same as (d–e) but for a
241   source station (open triangle) near Cistern.

242

243

244

3.2 Polarization Analysis

Following the algorithm described by Jurkevics (1988), the polarization analysis is performed to constrain the dominant direction of the particle motion at each receiver station for a given source station. A $n \times 3$ matrix, $\boldsymbol{C} = [\boldsymbol{ZZ}, \ \boldsymbol{ZN}, \ \boldsymbol{ZE}]$, is first constructed using the three-component hourly stacked CCFs (ZZ, ZN, and ZE), where n is the number of time sampling in the CCFs. To only focus on tremor signals generated by sources closer to the source station, we only use CCFs between 0 and positive 1.5 seconds lag time. The 3×3 covariance matrix $\boldsymbol{S}$ can then be constructed as

$$\boldsymbol{S} = \frac{\boldsymbol{C}^T \boldsymbol{C}}{n} \tag{1}.$$

The eigenvalues $(\lambda_1, \lambda_2, \lambda_3)$ and the normalized eigenvectors $(\boldsymbol{u_1}, \boldsymbol{u_2}, \boldsymbol{u_3})$ of $\boldsymbol{S}$ can be solved with the Singular Value Decomposition

$$(\boldsymbol{S} - \lambda_i \boldsymbol{I})\boldsymbol{u_i} = \boldsymbol{0}, \quad i = 1, 2, 3 \tag{2},$$

where $\boldsymbol{I}$ is the 3×3 identity matrix, $\boldsymbol{0}$ is the zero vector, and the eigenvalues are ordered as $\lambda_1 \geq \lambda_2 \geq \lambda_3$. The dominant polarized direction of the CCFs is the 3D eigenvector that corresponds to the largest eigenvalue, $\boldsymbol{u_1} = (u_{Z\_1}, u_{N\_1}, u_{E\_1})$. Based on $\boldsymbol{u_1}$, we obtain the azimuth ($tan^{-1}\left(\frac{u_{N\_1}}{u_{E\_1}}\right)$) and the incidence angle ($\cos^{-1}|u_{Z\_1}|$), which we can use to identify and locate the hydrothermal tremor sources.

Example results of polarization analysis for source stations closest to Steamboat and Cistern are shown in Figure 3. Before the eruption, clear isotropic radiation patterns are observed for both source stations (Figures 3d & 3i) with the majority of receivers pointing toward Steamboat and Cistern, respectively, inferring there are tremor sources beneath both features. For the source station near Cistern (Figure 3i), receivers nearby Steamboat are pointed toward Steamboat

268   instead of Cistern suggesting Steamboat tremor is stronger and the cross-correlation signal in the

269   negative lag interferes with the positive lag. When examing receivers close to the virtual sources,

270   incidence angles near Cistern (Figure 3i) are overall larger compared to Steamboat (Figure 3d)

271   suggesting that the Cistern source is closer to the surface. We note that this apparent depth

272   discrepancy could somewhat be offset by the elevation difference between the two features,

273   where Cistern is about 10 meters lower than Steamboat in elevation. After the eruption, clear

274   isotropic radiation patterns are again observed for the two source stations although the smaller

275   overall incidence angles indicate the deepening of the sources (Figures 3e & 3j). Moreover, the

276   center of the radiation pattern, the presumed source location, shifted about 60 meters toward the

277   southeast for the Cistern case. To determine the spatiotemporal distribution of the tremor

278   sources, we propose a two-step back projection process to progressively determine the source

279   distribution first in 2D and then in 3D.

280

281   **3.3 Surface Back Projection (2D)**

282   Instead of a direct 3D back-projection, for each source station, we first use the 10 closest receiver

283   stations to detect and locate the epicenter of the tremor sources in 2D space. Using only the

284   closest receivers avoids the potential interference from other sources and is effective in

285   identifying all potential tremor sources regardless of their strength. We create a 2D Cartesian

286   coordinate grid with 3-m spacing for the whole area, with each grid point representing a possible

287   epicenter of the tremor source location. The azimuth measured at each receiver from the

288   polarization analysis is projected as an infinite ray on the 2D surface (Figure 4a). Note that we

289   resolve the 180-degree ambiguity of the ray direction by assuming a down-going direction of the

290   eigenvector $\boldsymbol{u_1}$ (i.e., $u_{Z\_1} < 0$) as the presumed sources were located beneath the surface. The

291 orthonormal distance between each grid and the ray path can thus be calculated. For each grid

292 point, we determine the number of ray paths with the orthonormal distance smaller than 8 m.

293 When that number is higher than 50% (5 hits), we consider the grid point as a possible tremor
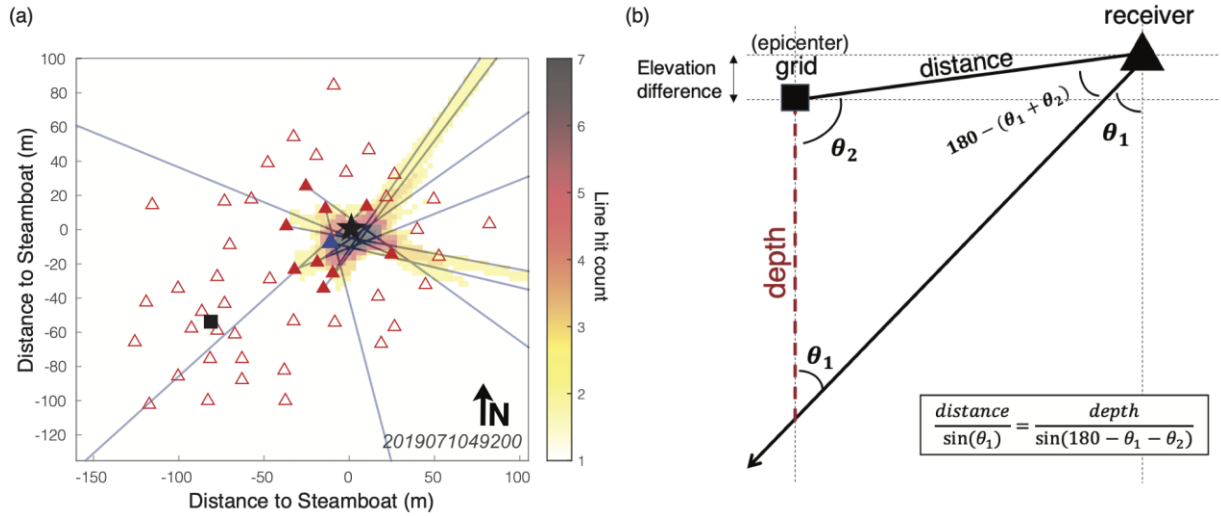
294 epicenter.

295

296

Figure 4. (a) An example of 2D surface back-projection of the polarization analysis
using 10 closest receiver stations (red-filled triangle) for a given source station (blue
triangle). Each line illustrates the azimuth measured at each receiver station from the
polarization analysis. The color-coded contours represent the density of the projected
lines. The epicenters (grid points) with line hit count over 5 will be saved for further
depth determination. The black star and square mark the Steamboat and Cistern
locations. (b) Depth determination accounting for the elevation difference based on the
trigonometric relationship marked in the lower-right box. θ_1 is the incidence angle
constrained by polarization analysis at receiver station and θ_2 is the incidence angle of
the grid-receiver vector.

307

308 As we expect a robust tremor epicenter should be inferred by multiple source stations nearby, we

309 remove all epicenter grid points inferred by only one or two source stations independent of time

310 from further analysis (Figure 5). As our interferometry method works best when source stations

311 are close to the tremor epicenters, we then further remove source stations that are 5 meters away

312   from the refined epicenter locations (Figure 5). This epicenter and station selection process can

313   be iterative and is marked as gray procedures in Figure 2. Note that we use a finer grid spacing (1

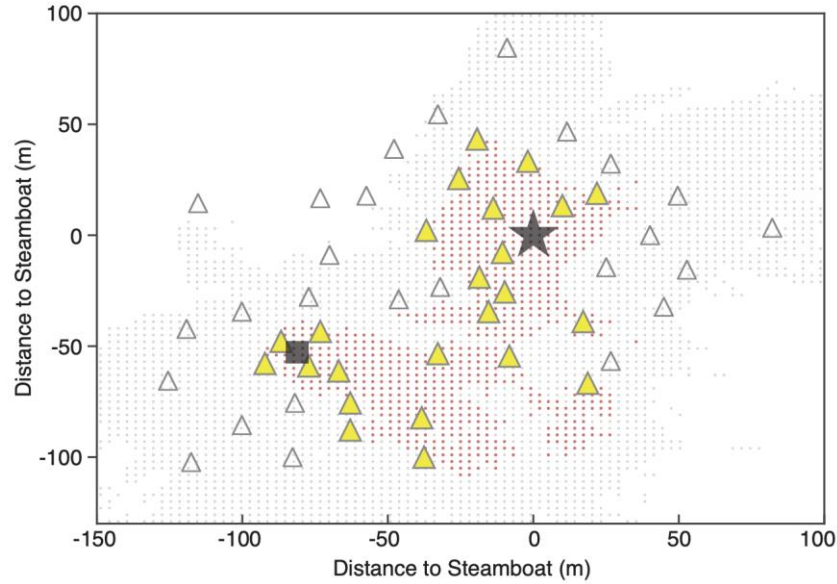314   m) in our 2nd iteration before proceeding to the 3D back-projection process discussed below.

315

Figure 5. The map of the potential tremor epicenters from the 1st iteration of the 2D
back-projection. The gray and red dots are the epicenters located by at least one and
three source stations, respectively. The selected source stations for the 2nd iteration are
marked as yellow triangles. The black star and square mark the Steamboat and Cistern
locations.

316
317
318
319
320
321

322

323   **3.4 Depth Back Projection (3D)**

324   A large array aperture is important for accurate source depth determination as the depth can be

325   better constrained with a wide range of incidence angles. Only P wave particle motion is useful,

326   however, as the incidence angle of a Rayleigh wave will always be more or less horizontal. To

327   determine the source depth, for each source station and each possible epicenter inferred by that

328   source station, we include all receivers with reliable P wave like motion. Here, we define P wave

329   like motion if the phase shift between the vertical and radial components of the CCFs is smaller

330   than 30 degrees (e.g., Figure 6). To preclude receivers with signals potentially interfered by other

331   sources, we impose a signal-to-noise ratio threshold of 5 on ZZ and require the azimuthal angle

332   to be within 90 degrees of the source epicenter. The signal-to-noise ratio is defined as the ratio

333   between the peak amplitude within the signal window (0 to 2 secs) and the root-mean-square

334   energy within the noise window (2 to 4 secs). For each receiver passing the selection criteria

335   above, the incidence angle is then used to determine the source depth with topography accounted

336   for based on the following trigonometric relationship

$$\frac{distance}{\sin(\theta_1)} = \frac{depth}{\sin(180 - \theta_1 - \theta_2)} \tag{3},$$

337   where the distance is the 3D distance between the epicenter grid and the receiver, θ_1 is the

338   incidence angle, θ_2 is the incidence angle of the grid-receiver vector (Figure 4b). The elevation is

339   taken from the high-resolution (0.5 m) Lidar data acquired from OpenTopography (ISB, 2009).

340   Note that this depth back projection approach assumes a homogeneous half space velocity

341   model. We consider this is a reasonable first-order approximation, given the relatively long-

342   wavelength of the 1–5 Hz seismic energy (compared to the depth we are investigating) but

343   further improvement can be done with the availability of a reference velocity model. For each

344   epicenter and a corresponding source station, we take the median depth among all the depths

345   inferred by all qualified receivers as the preliminary resolved depth. Then, we take the median

346   depth of the preliminary depths from different source stations as the best estimation of the source

347   depth for that grid (Figure 7). We note that all the measured tremor depths presented here and in

348   the following discussion are relative to Steamboat's elevation while Cistern's surface is ~10 m
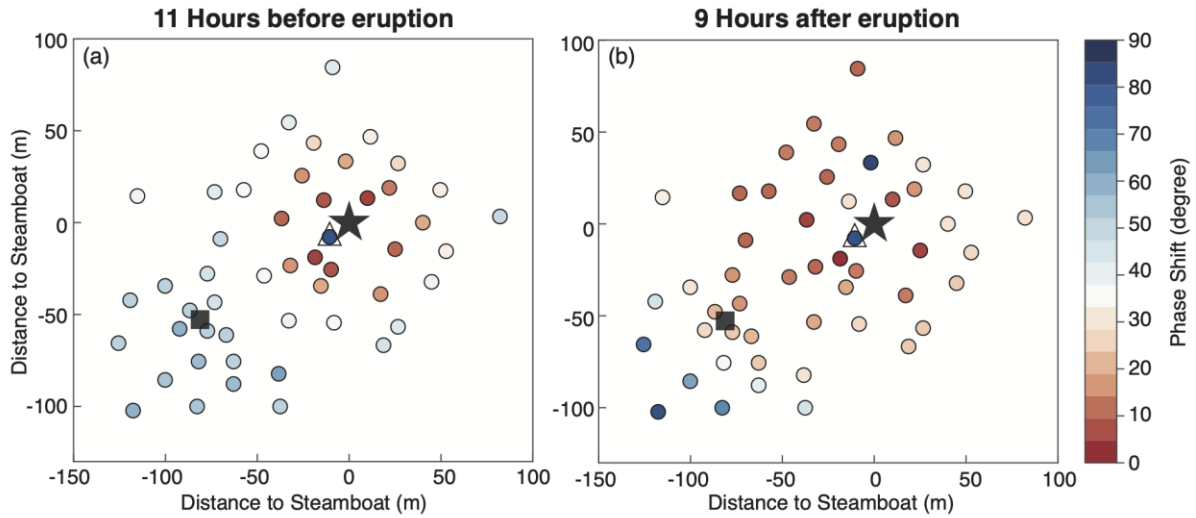
349   lower.

Figure 6. Measured phase shift between ZZ and ZR components of the cross-correlation functions around (a) 11 hours before and (b) 9 hours after the eruption. The common source station is denoted by the open triangle. We define P wave like motion as phase shift smaller than 30 degrees. The black star and square represent Steamboat and Cistern location, respectively.

4 Results

4.1 Spatiotemporal Distribution of the Tremor

By performing the polarization and back projection analyses for all the one-hour CCFs, we

observed systematic tremor source migration within the Steamboat/Cistern System throughout

the eruption cycles. Taking the eruption on 11 July 2019 as an example (Figure 7), around 11

hours before the eruption, the Steamboat and Cistern tremors were at ~25 and ~15 m depth,

respectively. At the onset of the eruption, the Steamboat tremor started to drop while Cistern

tremor remained at the same level. Nine hours after the eruption, both tremor sources dropped to

the deepest depths, with Steamboat tremor slightly shallower (~120 m) than Cistern tremor

(~140 m). Approximately 34 hours after the eruption, both tremor sources returned to the

shallow depths and stayed shallow until the next eruption. Throughout the eruption cycle, the

368   Steamboat tremor epicenters were persistently confined near the surficial vent indicating a near

369   vertical conduit. While persistent tremor sources are also observed directly beneath the Cistern

370   pool before the eruption, a considerable lateral shift is observed between 2 and approximate 30

371   hours after the eruption. This deep, laterally shifted, wide-spread area indicates a lateral turn and
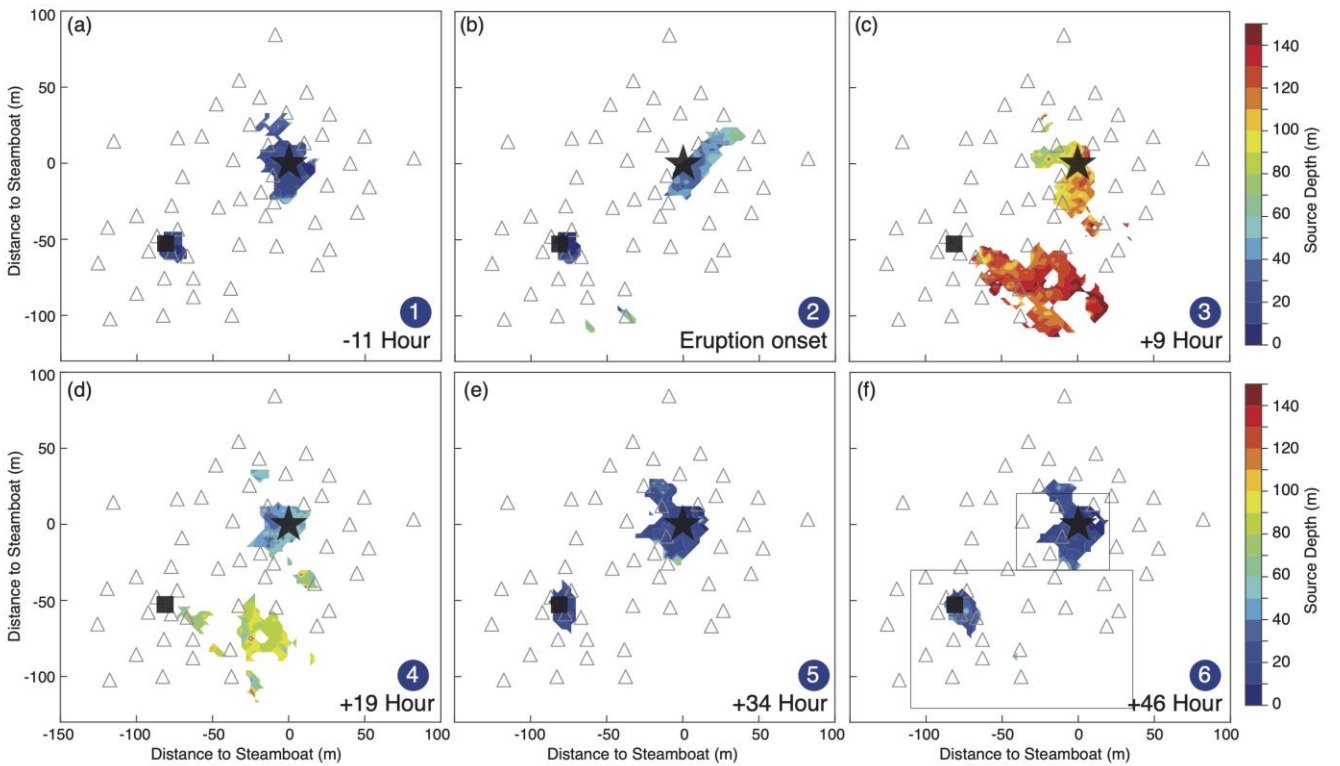
372   widening of the Cistern plumbing structure at depth.

373

374

Figure 7. The tremor source locations color-coded by the estimated depth. (a–f)
represent the six different stages (1–6; times relative to the eruption onset are shown in
the lower-right corners) during the eruption/recharge cycle based on the eruption on
July 11th 2019. The two open rectangles in (f) mark the areas for the averaged depth
calculation shown in Figure 9. The black star and square represent Steamboat and
Cistern location, respectively.

384 **4.2 Plumbing Architecture Outline**

385 As the tremor is assumed to originate from the steam/liquid phase transition within the water

386 column, the outline of all the possible tremor sources in 3D, independent of time, illuminates the

387 extent of the plumbing architecture. Here, to only illustrate the most robust 3D plumbing

388 features, we create the 3D isosurface plots (Figure 8) using a stricter than standard tremor source

389 selection criterion (i.e., with at least 80% hit count instead of 50% during the surface projected

390 analysis as described in section 3.3). While the fine scale structure is likely obscured by the

391 intrinsic resolution limit imposed by our array configuration and uncertainty associated with the

392 subsurface velocity structure, the 3D model nevertheless allows us to visualize the

393 Steamboat/Cistern subsurface plumbing complex for the first time. In particular, Figure 8

394 illustrates that the plumbing geometry beneath Steamboat is approximately vertical and extends

395 to at least ~120 m depth. The plumbing conduit beneath Cistern is vertical from the surface to

396 ~65 m depth. The bottom of the vertical conduit is laterally connected to the reservoir/cavity

397 between ~80 and at least ~140 m depth through an oblique and elongated conduit between ~65

398 and ~100 m depth. The center of the reservoir/cavity is ~60 m southeast of Cistern's surface

399 pool. Based on the structural continuity, hereafter we refer to Cistern's plumbing to be the

400 system as a whole, including the offset reservoir/cavity. Despite the fact that we know Cistern

401 and Steamboat are hydrologically connected, we do not observe any overlapping between their

402 tremor sources in space down to ~140 m depth. We hypothesize that the connection is likely

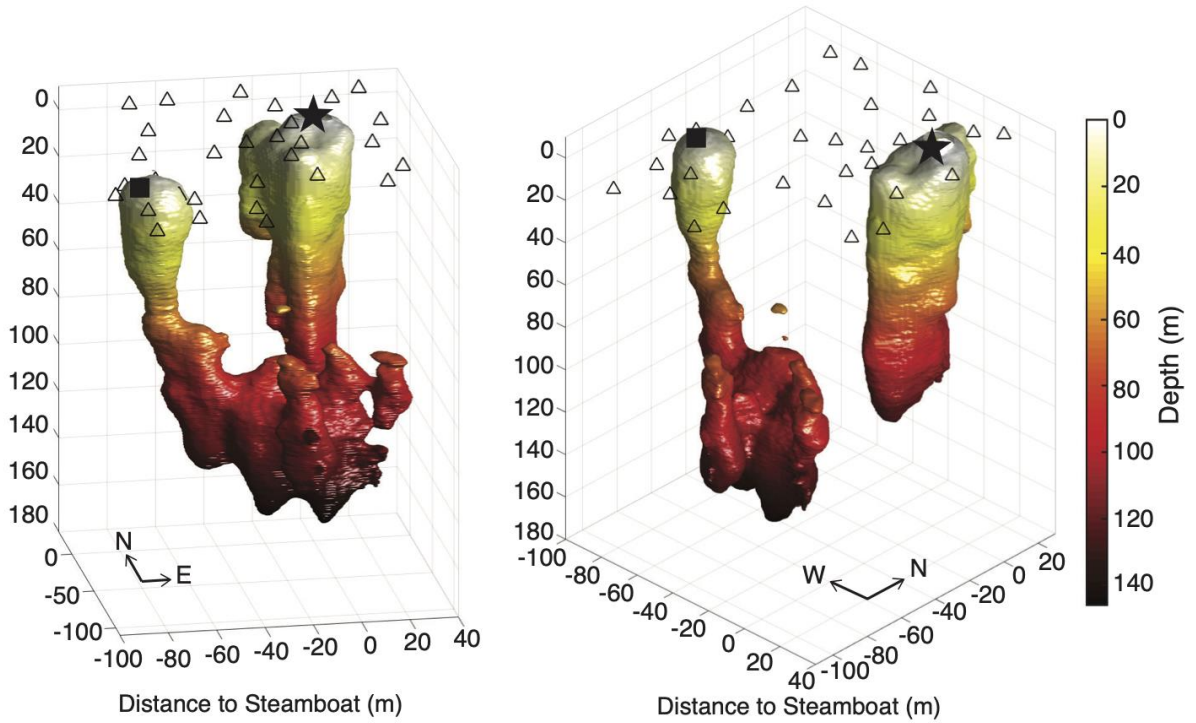403 aseismic, and/or is deeper than the current imaged depth.

404

Figure 8. The outline of the Steamboat and Cistern's plumbing with two viewing angles, inferred based on isosurface of the tremor source locations throughout the entire recorded cycles. The structure color-coded by the depth delineates the observed seismically active area during the eruption cycles. The solid star, solid square, and open triangles denote Steamboat, Cistern, and station locations on the surface, respectively.

4.3 Distinct Recharge Evolution Patterns

As the observed hydrothermal tremor were excited by the liquid/gas phase transition, the ability

to image the migration of the tremor sources hence allows us to track the phase transition

horizons of the Steamboat/Cistern system throughout the eruption cycles. From Figure 7 we can

see the tremor sources are somewhat clustered for both Steamboat and Cistern. To find the

centroid of the clusters, we first manually choose the source areas for Steamboat and Cistern (the

open rectangles in Figure 7). For each time and within each source area, we perform a grid

search to find a circle (with a 15-m radius) that contains the most abundant tremor source

420   locations. We then determine the depth based on the averaged depth of the tremor sources within

421   the resultant circle. Given the depth, in conjunction with the plumbing outline (Figure 8), we can

422   reproduce the complete recharge evolution of Steamboat and Cistern throughout the six eruption

423   cycles (Figure 9). Because the interval between eruptions (IBE) varied significantly (3–8 days)

424   during our data time period, here we summarize the general features that are common to all

425   eruptions.

426

427
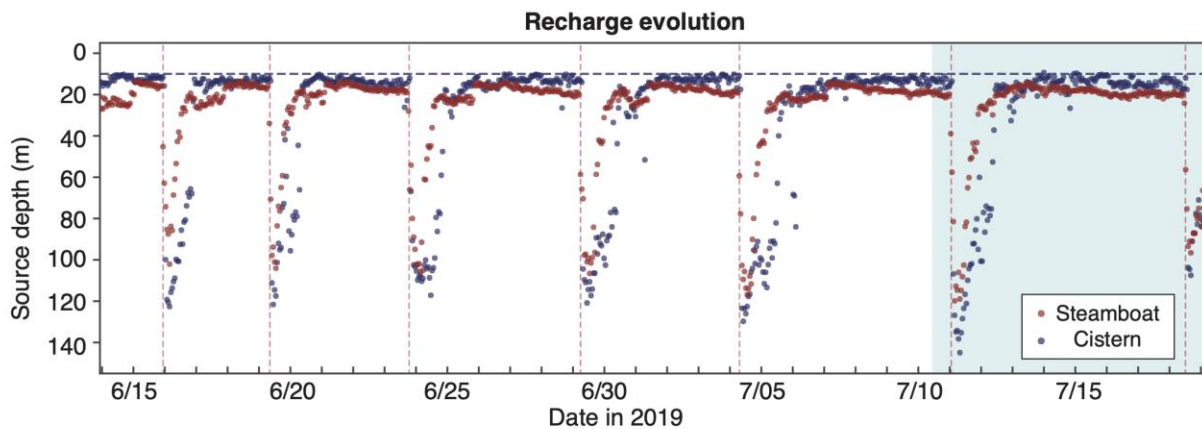
428   Figure 9. The temporal depth variation of Steamboat (red dots) and Cistern (blue dots)
429   tremor sources. The horizontal blue-dashed line represents the surface level of Cistern.
430   The vertical red-dashed lines mark the Steamboat eruption times. The light blue area
431   represents the enlargement time period shown in Figure 11.
432

433   Prior to eruptions, the phase-transition horizon was predominantly at ~25 m depth beneath

434   Steamboat. Although it was at ~15 m depth (relative to Steamboat vent), the phase-transition

435   horizon beneath Cistern was in fact much closer to the surface (<5 m) as Cistern is ~10 m lower

436   than the reference Steamboat elevation. Right after eruptions, the phase-transition horizon at

437   Steamboat dropped vertically in response to the heat and water evacuation and the potential cold

438   water refill through permeable medium (Munoz-Saez et al., 2015b), or the condensed steam

439   flowing back to the conduit (Hutchinson et al., 1997). In contrast, the phase-transition horizon at

440   Cistern did not drop until 1–2 hours later. About ~5–9 hours after eruptions, the phase-transition

441   horizons at both Steamboat and Cistern reached the deepest depth (>100 m), within the vertically

442   elongated conduit and the offset reservoir/cavity, respectively. Note that at this time the water

443   phase (<60 minutes) of the eruption had ceased already (White et al., 1988). After that, the

444   phase-transition horizons at Steamboat and Cistern both quickly ascended along the inferred

445   plumbing structures (Figure 8) and then slowed down when reaching 10–30 m depth. During the

446   migration, the phase-transition horizon at Steamboat was consistently shallower and reached the

447   10–30 m level hours earlier than Cistern. Finally, both phase-transition horizons remained at

448   shallow depths for days until the systems become primed for another eruption.

449

450   **5 Discussion**

451   **5.1 Contrasting Tremor Migration Rate between Steamboat and Cistern**

452   From the recharge evolution in Figure 9, we observe that Steamboat and Cistern have distinct but

453   related recharge progressions. To further quantify the interaction between the two, we highlight

454   four phases during the recharge that have distinct tremor migration rates for Steamboat and

455   Cistern (Figure 10). Phase I: At the onset of Steamboat's major eruptions, the Steamboat tremor

456   drops immediately, while Cistern tremor remains stagnant at surface level for 1–2 hours before

457   dropping to deeper depths. Phase II: In the first 20 hours after an eruption, Steamboat tremor

458   migrates upward at rates of more than two times faster than Cistern. Phase III: Between 20 and

459   30 hours after an eruption, Cistern's tremor migration rate is an order of magnitude faster than

460   Steamboat and is 3–4 times faster than it was in the first 20 hours. Phase IV: After 30–40 hours

461   post-eruption, both tremor sources return to shallower depths (~10–30 m deep) and stay at

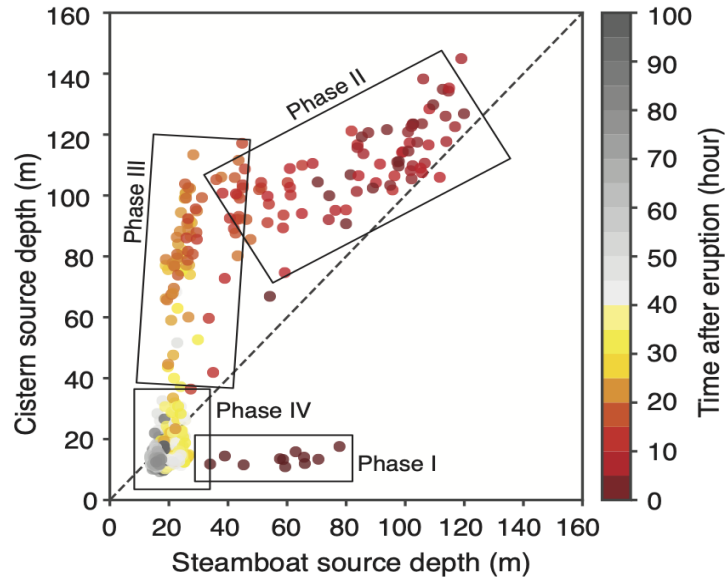462   similar levels for days until the next eruption.

463

Figure 10. The depth relationship between the Steamboat and Cistern tremor source
locations throughout the entire recorded period color-coded by the time after eruptions.
The four phases (I–IV) highlight the distinct characteristic of different depth migration
rates for Steamboat and Cistern tremor sources. As a reference, the diagonal gray-
dashed line marks the equal depth.

469

470

471   Assuming the heat influx is steady, the observed migration rate variation might indicate changes

472   in plumbing dimensions from deep to shallow, as heat can accumulate faster within a narrower

473   plumbing structure. For Cistern, the slow migration rate between 140 and 90 m depth during

474   Phase II likely reflects a large and expanded structure consistent with the wide-spread tremor

475   source area observed (Figures 7c and 8). The following faster migration rates (Phase III) thus

476   corresponds to the narrowing of the Cistern plumbing structure, which turns into a narrower

477   vertical conduit between ~90 m and ~20 m beneath Cistern (Figure 8). In Phase IV, the Cistern

478   migration rate slowed down considerably above ~20 m depth and eventually became stagnant

479   when nearly reaching the surface. At this shallow depth, the Cistern conduit gradually widens

480   toward the surface pool, and the heat influx from depth and heat diffusion at the pool surface are

481   likely close to equivalent. For Steamboat's plumbing, the fast migration rate in Phase II between

482   120 m and 30 m depth likely suggests a vertical conduit that is much smaller in size compared to

483   the Cistern reservoir/cavity (Figure 8). It is unclear why Steamboat tremor sources stay at 20–30

484   m depth for days prior to the eruption (Phase IV). This depth might be somehow controlled by

485   the elevation difference between Steamboat and Cistern but we cannot rule out the existence of a

486   shallow reservoir or a bubble trap feature that enables two-phase mixture (Vandemeulebrouck et

487   al., 2014). Note that this 20–30 m tremor depth before eruptions is slightly deeper than the ~20 m

488   depth observed at Old Faithful (Wu et al., 2019), which might cause the greater heights of

489   Steamboat eruptions (Reed et al., 2019).

490

491   **5.2 Comparison with In Situ Pressure and Temperature Data**

492   It is still enigmatic why Cistern has a late response (Phase I) to a major eruption of Steamboat's

493   and how these two systems are connected. With the availability of the in situ pressure and

494   temperature measurements placed within Cistern's pool (~3.5 m depth), we can better understand

495   how Cistern relates to Steamboat by closely comparing the physical state of the Cistern pool with

496   the tremor evolution (Figure 11). At the onset of eruption, temperature at Cistern pool dropped

497   (less than a half degree [ºC]) immediately but the water level was steady and kept boiling for 1–2

498   hours, consistent with the observed shallow Cistern tremor depth during Phase I (Figures 7b and

499   10). This apparent delay in response for Cistern to Steamboat eruptions indicates that the two

500   features might not connect through an open pipe structure but perhaps through a diffusive porous

501   media (Ingebritsen and Rojstaczer, 1993; Munoz-Saez et al., 2015b), where the permeable flow

502   is driven by the hydrostatic pressure gradient. The immediate temperature decrease is likely the

503   result of immediate reduction of heat influx from deep resulting from Steamboat's major
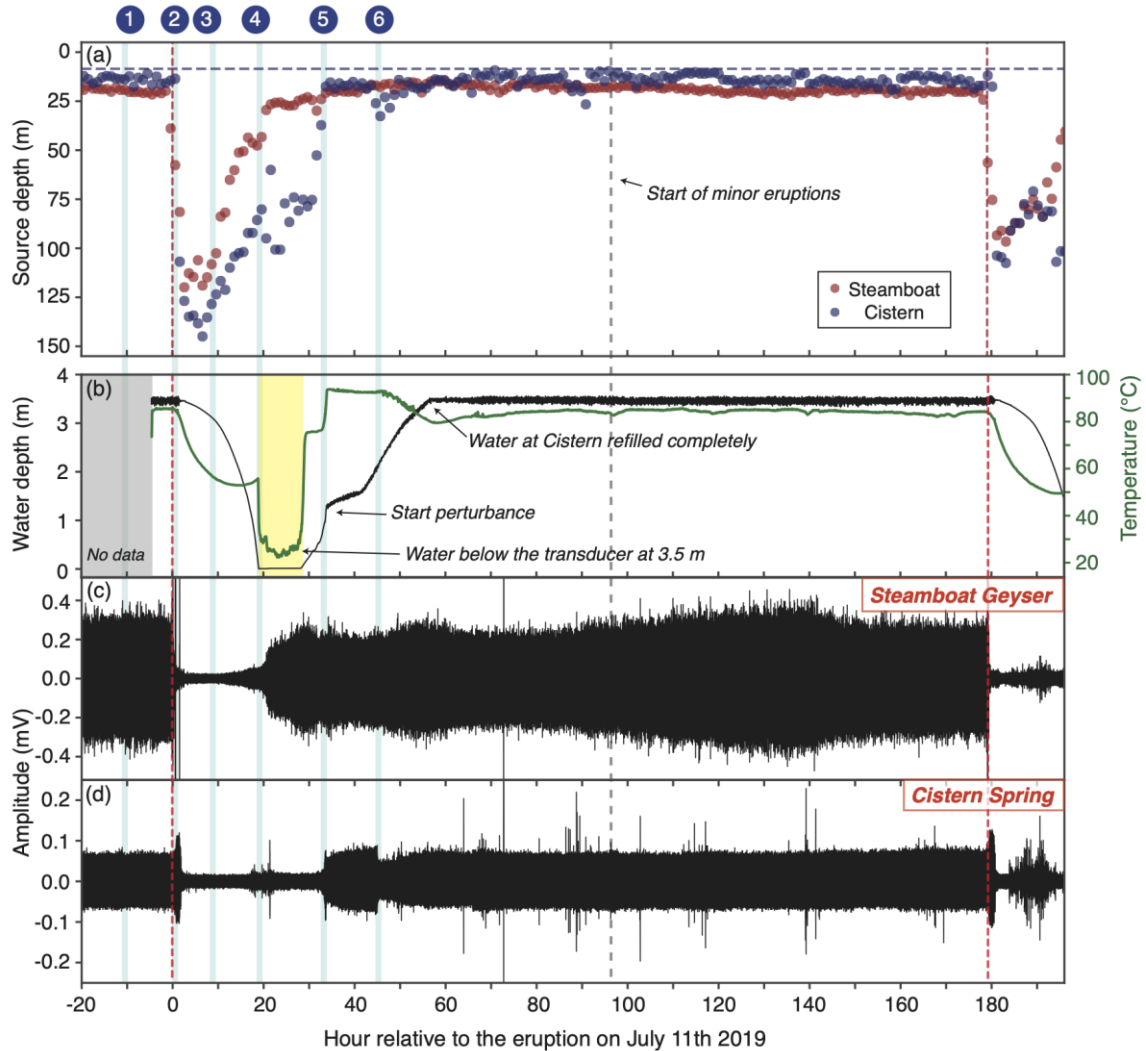
504   eruption.

505

Figure 11. (a) Comparison between tremor depths, (b) in situ water level (black) and
temperature (green) measurements at 3.5 m depth within the Cistern pool, and (c–d)
the 1–5 Hz tremor amplitudes observed near Steamboat and Cistern for the Steamboat
eruption cycle on 11 July 2019 (light blue time window in Figure 9). The red-dashed
lines mark the eruption times. Blue vertical lines highlight six different stages during the
eruption/recharge cycle with distinguished measurement characteristics also shown in
Figures 7a–7f. The gray and yellow areas mark the time windows when the in situ data
is not available and water level dropped below the transducer, respectively.

515

516

517   About 1–2 hours after eruption onset, the water level at Cistern pool gradually drops and takes

518   ~20 hours to drop >3.5 meters (below the transducer). Around this time, Steamboat tremor raises

519   to about 30 m depth coinciding with the tremor amplitude increase observed at the surface.

520   Intriguingly, this time coincides with the oscillation of Cistern tremor and the spontaneous

521   increase in Cistern seismic amplitude (stage 4 in Figure 11). Around 10 hours later (30 hours

522   after eruption), the water at Cistern gradually refills surpassing the 3.5 m level and starts to boil

523   at ~2 m level a few hours later. The boiling is consistent with both the migration of Cistern

524   tremor to a shallower depth and the increase tremor amplitude at the surface (Figure 11d).

525   Around 45 hours after the eruption, a sudden decrease in Cistern seismic amplitude that

526   corresponds to the drops of both tremor depth and the water temperature is observed. Note that

527   the pressure data consistently indicates water disturbance (boiling) while the temperature has

528   dropped below the boiling temperature (93 °C), suggesting the pool was thermally stratified and

529   the boiling is occurring somewhere deeper than the transducer. Overall the observed tremor

530   migration and amplitude at Cistern are remarkably consistent with the appearance of water level

531   and the boiling status within Cistern's pool. Around 55 hours post-eruption, Cistern is

532   completely refilled and overflowing until the next major eruption, with no clear change in the

533   physical state related to Steamboat's minor eruption activity.

534

535   The delay of tremor migration (both descending and ascending) combined with the insensitivity

536   of Cistern to Steamboat's minor eruptions, again indicates that the two features are probably not

537   connected through an open channel that fluid can circulate freely. On the other hand, no

538   significant Steamboat tremor depth variation has been observed corresponding to the resumption

539   of minor eruptive activity. This suggests the minor eruptions are mostly controlled by shallow

540   dynamic processes and do not involve the deeper part of the plumbing system. Further thermal

541   dynamic modeling will be needed to provide more insights into the interaction between

542   Steamboat and Cistern as well as the eruption dynamics of the Steamboat system. That is,

543   however, beyond the scope of this current study.

544

545   **5.3 Steamboat's Predictability?**

546   Steamboat is an episodic but not periodic geyser. During the current active phase since March

547   2018, the interval between eruptions (IBE) has changed by an order of magnitude from 3 to 35

548   days. It is interesting and enigmatic about, whether Steamboat eruptions are stochastic or

549   deterministic, and if deterministic, whether Steamboat eruptions can be predicted. For the

550   predictable geyser such as Old Faithful, its periodic eruptions are considered as the outcome of

551   thermodynamic equilibrium, where the minor errors (10–15% of the eruption interval) may come

552   from a stochastic component. Like Old Faithful, previous geyser prediction schemes are

553   developed based on periodicity of the surface activity (Eibl et al., 2020; Gouveia & Friedmann,

554   2006). To our best knowledge, no prediction has ever been attempted on "non-regular" geysers

555   such as Steamboat. Therefore, using the nodal data, we could firstly explore the geyser

556   predictability via its internal behavior. One caveat is that the nodal deployment was restricted by

557   battery power so that only six eruption cycles are recorded as Steamboat has overall longer time

558   scales (hours to days) for its recharge and eruptive activity compared to other studied periodic

559   geysers (seconds to minutes; e.g., Eibl et al., 2020; Munoz-Saez et al., 2015a, 2015b; Rinehart,

560   1965). Nevertheless, the recorded IBE varied significantly from 3 to 8 days, which, we consider

561   still can be a good proxy as a pilot study.

562

563 From the recharge evolution, we observe a positive relationship between the deepest tremor

564 depth and the IBEs (Figure 12a). The variation of the deepest tremor depth can be attributed to

565 the various amount of energy evacuated from eruptions, hence the correlation with IBEs may

566 suggest that Steamboat's system has a steady heat influx, and the eruptions are due to the

567 outcome of equilibrium. Interestingly, there are two parameters positively correlated with the

568 deepest tremor depth: the time duration for tremor migration from deepest depth to shallow and

569 the minor eruption duration (Figures 12b & 12c). Both time durations are lengthened when the

570 tremor dropped to deeper. The longer migration time is reasonable considering the steady heat

571 influx, and we speculate the minor eruption duration is modulated by the waiting time for the

572 shallow reservoir to be sufficiently heated and primed for an eruption (Namiki et al., 2016).

573 Because the 1–5 Hz seismic amplitude increases sharply when the tremor returns to shallower

574 depths (Figure 11c), data from a single station may offer sufficient information for prediction

575 and collecting continuous data successively over a long time period becomes possible. Combing

576 the minor eruption time (from a temperature logger in Steamboat's run off channel), it is possible

577 to statistically evaluate Steamboat's predictability, which will be the subject of future studies.
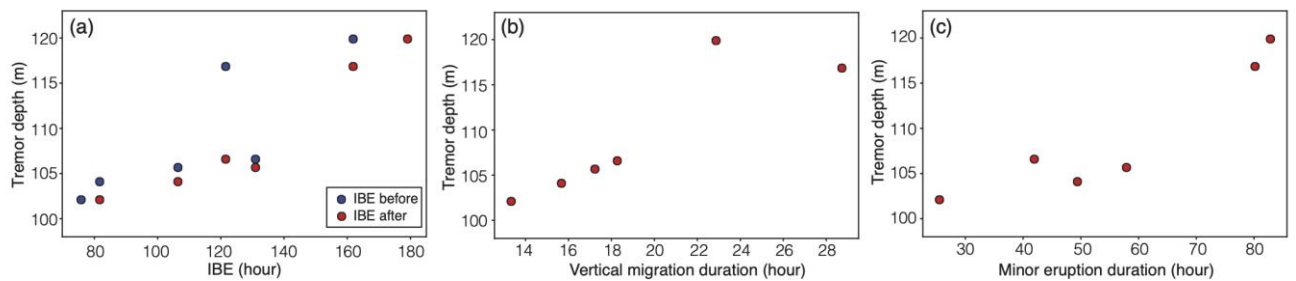
578

579 Figure 12. The relationship between the deepest tremor depth after the eruption and (a)
580 the interval between eruption (IBE), (b) the vertical migration durations from the deepest
581 depth to shallow, and (c) minor eruption duration. The IBE before and after represent
582 the intervals to the previous and the next eruption, respectively.

583

584 **6 Conclusion**

585 To understand the underground architecture and the eruption/recharge dynamics of Steamboat

586 and Cistern, we deployed a dense 3-component nodal array in the vicinity of Steamboat and

587 Cistern between June and July 2019. From the continuous recordings, we observed distinct low-

588 frequency hydrothermal tremors excited by liquid/gas phase transition within both Cistern and

589 Steamboat. These tremors are clearly associated with the Steamboat's eruption cycle, and

590 showed no isolated events and discernable arrivals. To constrain the spatiotemporal location of

591 the tremor, we developed a new method that combines multicomponent cross-correlation,

592 polarization analysis, and 2D then 3D progressive back projections. Results of mapping the 3D

593 tremor source locations successfully outlines Steamboat and Cistern's plumbing structure down

594 to 140 meter depth. Steamboat's plumbing is approximately vertical and extends to at least ~120

595 m depth. The conduit beneath Cistern is vertical from the surface to ~65 m then connected to a

596 large and lateral offset reservoir down to ~140 m depth through an oblique conduit. Seismically,

597 we observe no clear physical connections between Steamboat and Cistern. Tracking the depth

598 horizon of the tremor migration, we reveal the recharge evolution and interaction of Steamboat

599 and Cistern throughout the eruption cycles with hourly resolution. Tremor sources within both

600 features dropped to depths >100 m after the eruption and tremor sources gradually shallowed

601 following the warming of the systems, then stayed at shallow levels for days until the next

602 eruption. The exact depths and the migration rates are distinct, however, for Steamboat and

603 Cistern indicating the two systems are likely connected through a porous medium instead of open

604 channels.

605

606 **Acknowledgments**

614

615 **References**

616 Adelstein, E., Tran, A., Saez, C. M., Shteinberg, A., & Manga, M. (2014). Geyser preplay and

617   eruption in a laboratory model with a bubble trap. *Journal of Volcanology and*

618   *Geothermal Research, 285*, 129-135.

619 Ardid, A., Vera, E., Kelly, C., Manga, M., Munoz-Saez, C., Maksymowicz, A., & Ortega-

620   Culaciati, F. (2019). Geometry of geyser plumbing inferred from ground deformation.

621   *Journal of Geophysical Research: Solid Earth, 124*, 1072–1083.

622   https://doi.org/10.1029/2018JB016454

623 Belousov, A., Belousova, M., & Nechayev, A. (2013). Video observations inside conduits of

624   erupting geysers in Kamchatka, Russia, and their geological framework: Implications for

625   the geyser mechanism. *Geology, 41*(4), 387-390.

626 Bowden, D., Tsai, V., & Lin, F. (2015). Site amplification, attenuation, and scattering from

627   noise correlation amplitudes across a dense array in Long Beach, CA. *Geophysical*

628   *Research Letters, 42*(5), 1360-1367.

629   Caylor, J. R. (2020). "Shallow Seismic Modeling Of The Hydrothermal Plumbing System

630   Beneath Old Faithful Geyser In The Upper Geyser Basin Of Yellowstone National

631   Park". *Open Access Theses & Dissertations*. 2945.

632   https://scholarworks.utep.edu/open_etd/2945

633   Carr, B., Sims, K. W., Ciraula, D., & Bouligand, C. (2019). What Does Old Faithful Look Like

634   Below the Surface and Why is it There? New Hydrogeophysical and Time-Lapse

635   Imaging of Old Faithful, Yellowstone National Park. *AGU Fall Meeting Abstracts*,

636   V24B-02.

637   Eibl, E. P. S., Hainzl, S., Vesely, N. I. K., Walter, T. R., Jousset, P., Hersir, G. P. & Dahm, T.

638   (2020). Eruption interval monitoring at Strokkur Geyser, Iceland. *Geophysical Research

639   Letters, 47*, e2019GL085266. https://doi.org/10.1029/2019GL085266

640   Farrell, J., & Lin, F.-C. (2019). Steamboat Geyser Nodal Experiment 2019 [Data set].

641   International Federation of Digital Seismograph Networks.

642   https://doi.org/10.7914/SN/9N_2019

643   GeyserTimes (2020), Eruptions of Steamboat Geyser 2018–2020 [online database]. Available

644   from http://www.geysertimes.org/archive/

645   Gomberg, J. S., Shedlock, K. M., & Roecker, S. W. (1990). The effect of S-wave arrival times

646   on the accuracy of hypocenter estimation. *Bulletin of the Seismological Society of

647   America, 80*(6A), 1605-1628.

648   Gouveia, F. J., & Friedmann, S. J. (2006). Timing and prediction of CO2 eruptions from Crystal

649   Geyser, UT (No. UCRL-TR-221731). Lawrence Livermore National Lab.(LLNL),

650   Livermore, CA (United States).

651   Guo, H., Zhang, H., Nadeau, R. M., & Peng, Z. (2017). High-resolution deep tectonic tremor

652   locations beneath the San Andreas Fault near Cholame, California, using the double-pair

653   double-difference location method. *Journal of Geophysical Research: Solid Earth,*

654   *122*(4), 3062-3075.

655   Hurwitz, S., & Manga, M. (2017). The Fascinating and Complex Dynamics of Geyser

656   Eruptions. *Annual Review of Earth and Planetary* Sciences *45*(1), 31–59.

657   https://doi.org/10.1146/annurev-earth-063016-015605

658   Hutchinson, R. A., Westphal, J. A., & Kieffer, S. W. (1997). In situ observations of Old Faithful

659   geyser. *Geology, 25*(10), 875-878.

660   Ingebritsen, S. E., & Rojstaczer, S. A. (1993). Controls on geyser periodicity. *Science,*

661   *262*(5135*)*, 889-892.

662   ISB (2009). EarthScope Intermountain Seismic Belt LiDAR Project. NCALM, UNAVCO,

663   EarthScope, and National Science Foundation, distributed by OpenTopograohy.

664   https://doi.org/10.5069/G9VD6WCS

665   Jurkevics, A. (1988). Polarization analysis of three-component array data. *Bulletin of the*

666   *Seismological Society of America, 78*(5), 1725-1743.

667   Kao, H., & Shan, S. J. (2004). The source-scanning algorithm: Mapping the distribution of

668   seismic sources in time and space. *Geophysical Journal International, 157*(2), 589-594.

669   Karlstrom, L., Hurwitz, S., Sohn, R., Vandemeulebrouck, J., Murphy, F., Rudolph, M.

670   L.,…McCleskey, R. B. (2013). Eruptions at Lone Star Geyser,Yellowstone National

671   Park, USA: 1. Energetics and eruption dynamics. *Journal of Geophysical Research, 118*,

672   4048–4062. https://doi.org/10.1002/jgrb.50251

673   Kedar, S., Sturtevant, B., & Kanamori, H. (1996). The origin of harmonic tremor at Old Faithful

674   Geyser. *Nature, 379*(6567), 708–711.

675   Kedar, S., Kanamori, H., & Sturtevant, B. (1998). Bubble collapse as the source of tremor at

676   Old Faithful Geyser. *Journal of Geophysical Research: Solid Earth, 103*(B10), 24283-

677   24299.

678   Kieffer, S. W. (1984). Seismicity at Old Faithful Geyser: an isolated source of geothermal noise

679   and possible analogue of volcanic seismicity. *Journal of Volcanology and Geothermal*

680   *Research, 22*(1-2), 59-95.

681   Kieffer, S. W. (1989). Geologic nozzles. *Reviews of Geophysics, 27*(1), 3-38.

682   Lin, F.-C., Tsai, V. C., & Schmandt, B. (2014). 3-D crustal structure of the western United

683   States: application of Rayleigh-wave ellipticity extracted from noise cross-

684   correlations. *Geophysical Journal International, 198*(2), 656-670.

685   Lynne, B. Y., Heasler, H., Jaworowski, C., Smith, G. J., Smith, I. J., & Foley, D. (2018).

686   Ground penetrating radar documents short-term near-surface hydrological changes

687   around Old Faithful Geyser, Yellowstone National Park, USA. *Journal of Volcanology*

688   *and Geothermal Research, 354*, 1-12.

689   Munoz-Saez, C., Manga, M., Hurwitz, S., Rudolph, M. L., Namiki, A., & Wang, C. Y. (2015a).

690   Dynamics within geyser conduits, and sensitivity to environmental perturbations:

691   insights from a periodic geyser in the El Tatio geyser field, Atacama Desert, Chile.

692   *Journal of Volcanology and Geothermal Research, 292*, 41–55.

693   https://doi.org/10.1016/j.jvolgeores.2015.01.002

694   Munoz-Saez, C., Namiki, A., & Manga, M. (2015b). Geyser eruption intervals and interactions:

695   examples from El Tatio, Atacama, Chile. *Journal of Geophysical Research: Solid Earth,*

696   *120*, 7490–7507. https://doi.org/10.1002/2015JB012364

697   Namiki, A., Ueno, Y., Hurwitz, S., Manga, M., Munoz-Saez, C., & Murphy, F. J. G. (2016). An

698   experimental study of the role of subsurface plumbing on geothermal discharge.

699   *Geochemistry, Geophysics, Geosystems, 17*(9), 3691–3716.

700   https://doi.org/10.1002/2016GC006472

701   Price, A.N., Lindsey, C., Fairley, J.P., and Larson, P.B.: Imaging Near-Surface Controls on Hot

702   Spring Expression Using Shallow Seismic Refraction in Yellowstone National Park:

703   *AGU Fall Meeting Abstracts*, V12B-01.

704   Reed, M. H., Barth, A., Girona, T., Hajimirza, S., Hurwitz, S., Karlstrom, L., Karplus, M. S.

705   Manga, M., Muñoz-Saez, C., Rashtbehesht, S. H., & Wu, S. M. (2019). Multiparameter

706   Study of Eruptive Behavior at Steamboat Geyser, Yellowstone. *AGU Fall Meeting,*

707   *Abstract,* V33D-0196.

708   Rinehart, J. S. (1965). Earth tremors generated by Old Faithful geyser. *Science, 150*(3695), 494-

709   496.

710   Richards, P. G., Waldhauser, F., Schaff, D., & Kim, W. Y. (2006). The applicability of modern

711   methods of earthquake location. *Pure and Applied Geophysics, 163*(2-3), 351-372.

712   Rudolph, M. L., & Sohn, R. A. (2017). A model for internal oscillations in geysers, with

713   application to Old Faithful (Yellowstone, USA). *Journal of Volcanology and*

714   *Geothermal Research, 343*, 17-24.

715   Rudolph, M. L., Sohn, R. A., & Lev, E. (2018). Fluid oscillations in a laboratory geyser with a

716   bubble trap. *Journal of Volcanology and Geothermal Research, 368*, 100-110.

717   Shapiro, N. M., Campillo, M., Stehly, L., & Ritzwoller, M. H. (2005). High-resolution surface-

718   wave tomography from ambient seismic noise. *Science, 307*(5715), 1615-1618.

719   Vandemeulebrouck, J., Roux, P., & Cros, E. (2013). The plumbing of Old Faithful Geyser

720   revealed by hydrothermal tremor. *Geophysical Research Letters, 40*(10), 1989-1993.

721   Vandemeulebrouck, J., Sohn, R. A., Rudolph, M. L., Hurwitz, S., Manga, M., Johnston, M. J.,

722   Soule, A., McPhee, D., Glen, J. M., Karlstrom, L., & Murphy, F. (2014). Eruptions at

723   Lone Star geyser, Yellowstone National Park, USA: 2. Constraints on subsurface

724   dynamics. *Journal of Geophysical Research: Solid Earth, 119*(12), 8688-8707.

725   Walter, T. R., Jousset, P., Allahbakhshi, M., Witt, T., Gudmundsson, M. T., & Hersir, G. P.

726   (2018). Underwater and drone based photogrammetry reveals structural control at Geysir

727   geothermal field in Iceland. *Journal of Volcanology and Geothermal Research, 391*.

728   https://doi.org/10.1016/j.jvolgeores.2018.01.010

729   Wu, S.-M., Ward, K. M., Farrell, J., Lin, F.-C., Karplus, M., & Smith, R. B. (2017). Anatomy of

730   Old Faithful from subsurface seismic imaging of the Yellowstone Upper Geyser

731   Basin. *Geophysical Research Letters, 44*(20).

732   Wu, S.-M., Lin, F.-C., Farrell, J., & Allam, A. (2019). Imaging the deep subsurface plumbing of

733   Old Faithful geyser from low-frequency hydrothermal tremor migration. *Geophysical

734   Research Letters, 46*. https://doi.org/10.1029/2018GL081771

735   White, D. E., Fournier, R. O., Muffler, L. J. P., & Truesdell, A. H. (1975). Physical results of

736   research drilling in thermal areas of Yellowstone National Park, Wyoming, U.S.

737   Geological Survey Professional Paper 892 (pp. 70).

738   White, D. E., R. A. Hutchinson, & T. E. C. Keith (1988), The Geology and Remarkable

739   Thermal Activity of Norris Geyser Basin, Yellowstone National Park, Wyoming, USGS

740   Professional Paper 1456.

741   Wicks, C. W., Dzurisin, D., Lowenstern, J. B., & Svarc, J. (2020). Magma intrusion and volatile

742   ascent beneath Norris Geyser Basin, Yellowstone National Park. *Journal of Geophysical*

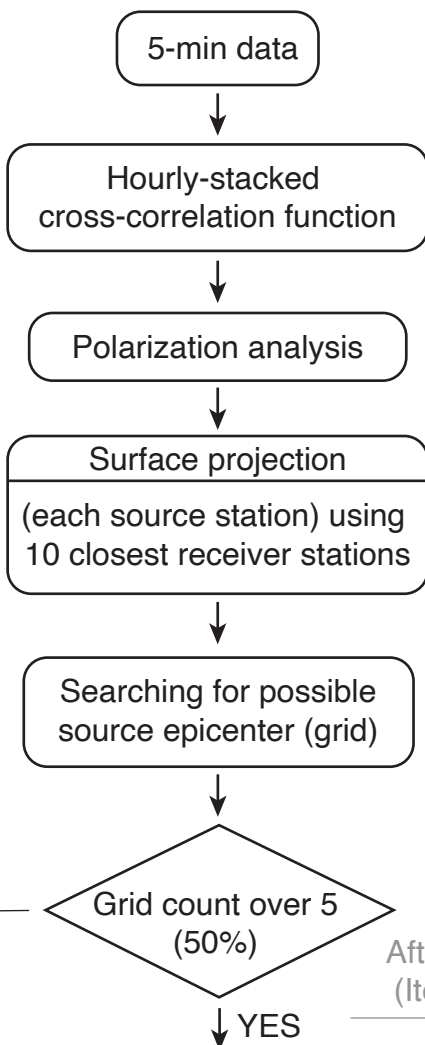743   *Research: Solid Earth, 125*. https://doi.org/10.1029/2019JB018208
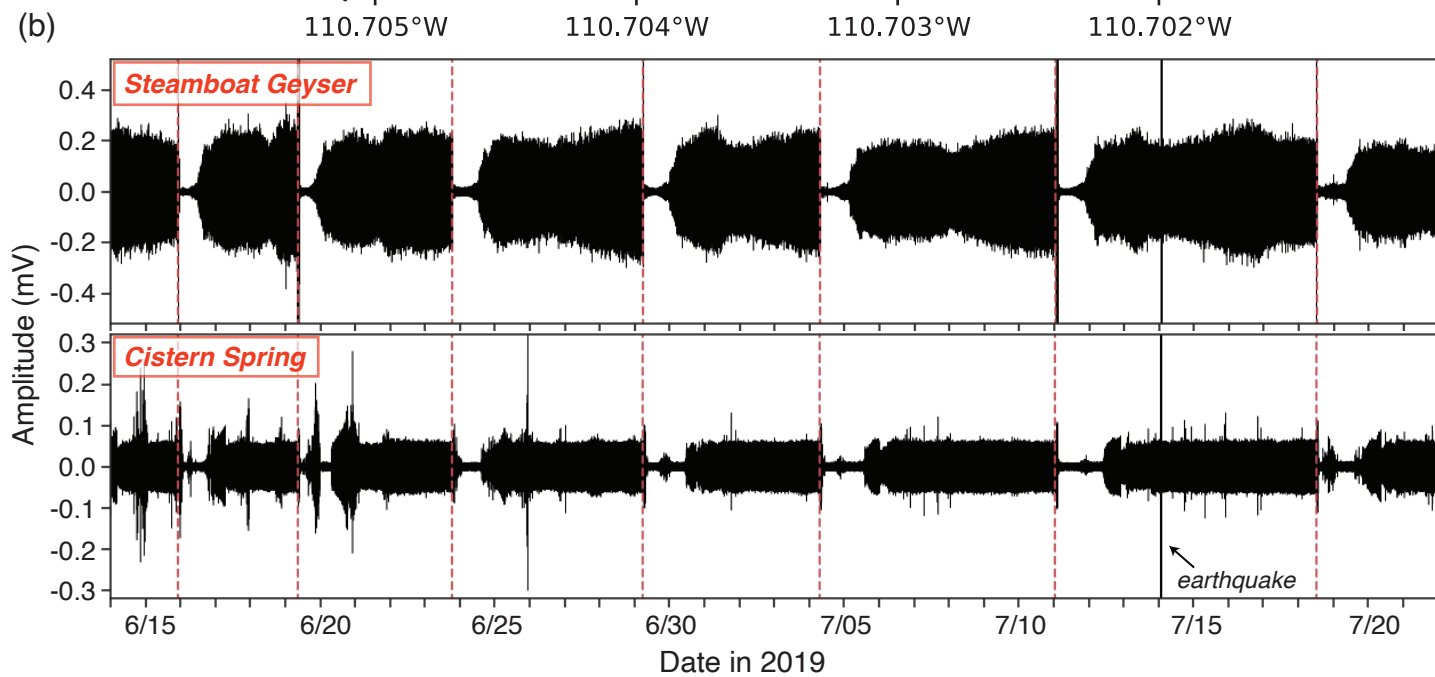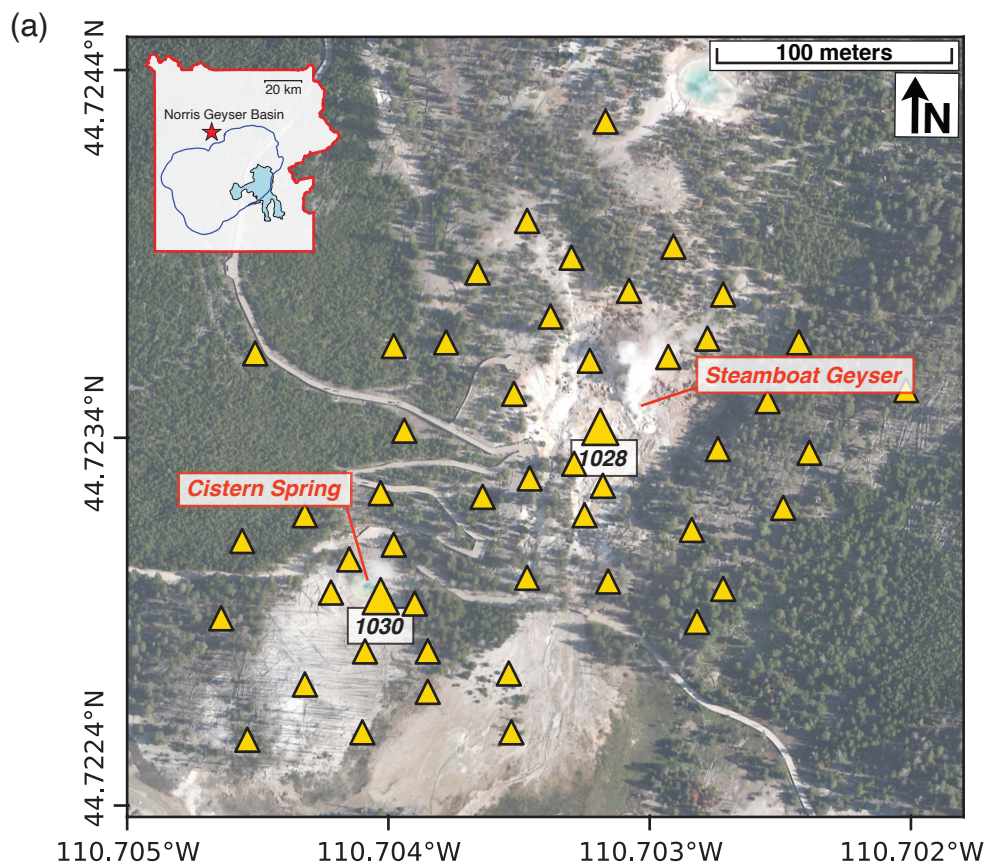
Figure1.

(a)

100 meters

N

Norris Geyser Basin

20 km

44.7244°N

44.7234°N

44.7224°N

Steamboat Geyser

Cistern Spring

1028

1030

110.705°W   110.704°W   110.703°W   110.702°W

(b)

Steamboat Geyser

Cistern Spring

earthquake

0.4
0.2
0.0
-0.2
-0.4

0.3
0.2
0.1
0.0
-0.1
-0.2
-0.3

Amplitude (mV)

6/15   6/20   6/25   6/30   7/05   7/10   7/15   7/20

Date in 2019

Figure2.

Figure3.

Figure showing amplitude vs. lag time plots (a-c, f-h) and spatial distributions of incidence angle "11 Hours before eruption" (d, i) and "9 Hours after eruption" (e, j).

Figure4.

(a)

(b)

$$\frac{distance}{\sin(\theta_1)} = \frac{depth}{\sin(180 - \theta_1 - \theta_2)}$$

Figure5.

Distance to Steamboat (m)
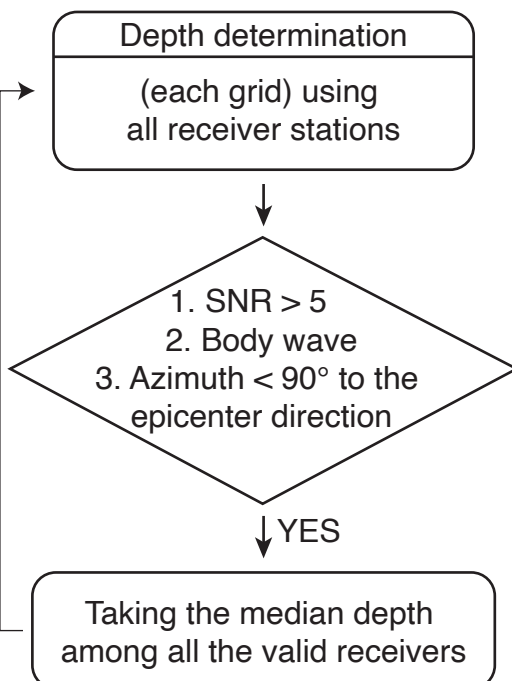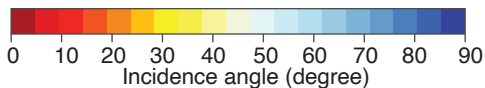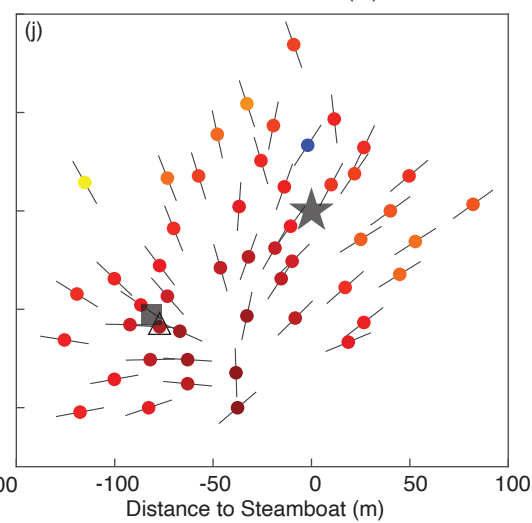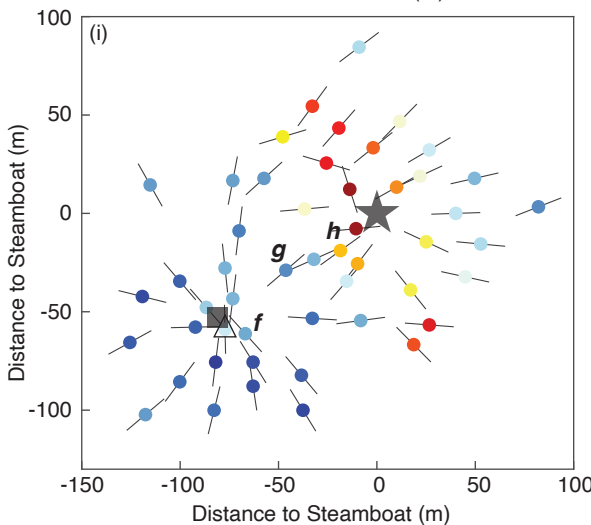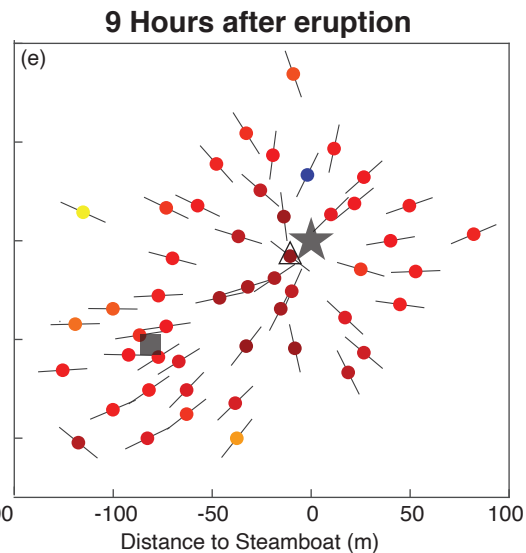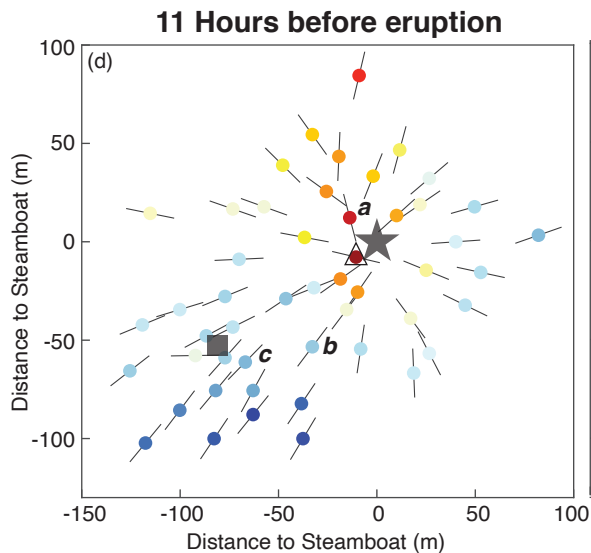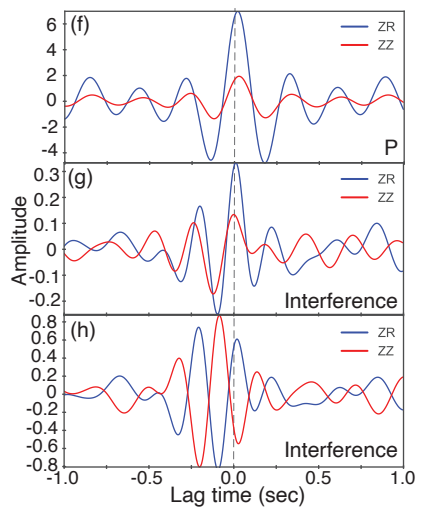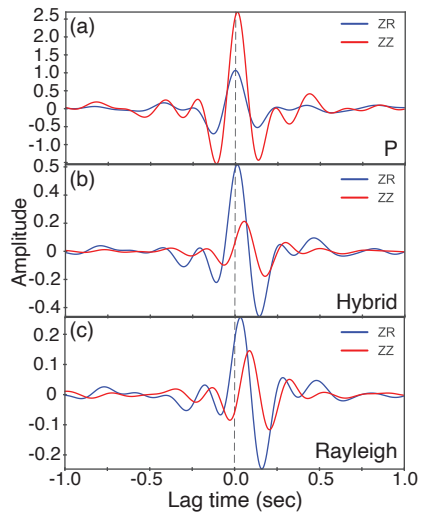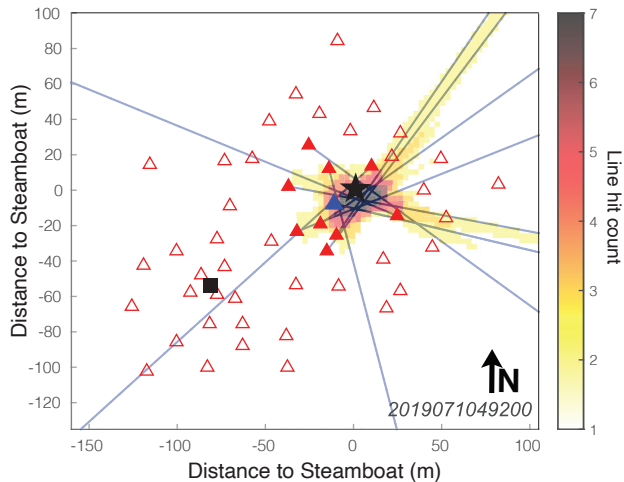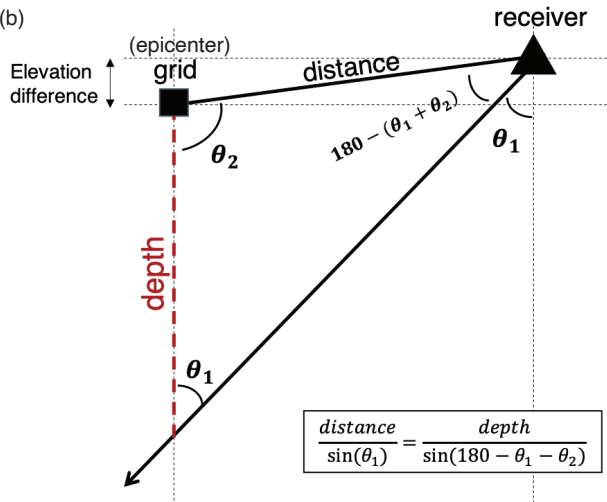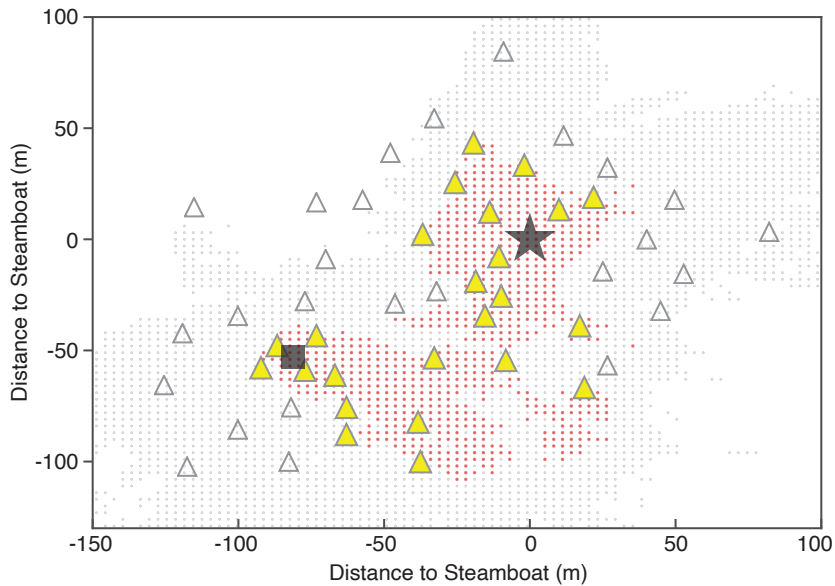
Figure6.

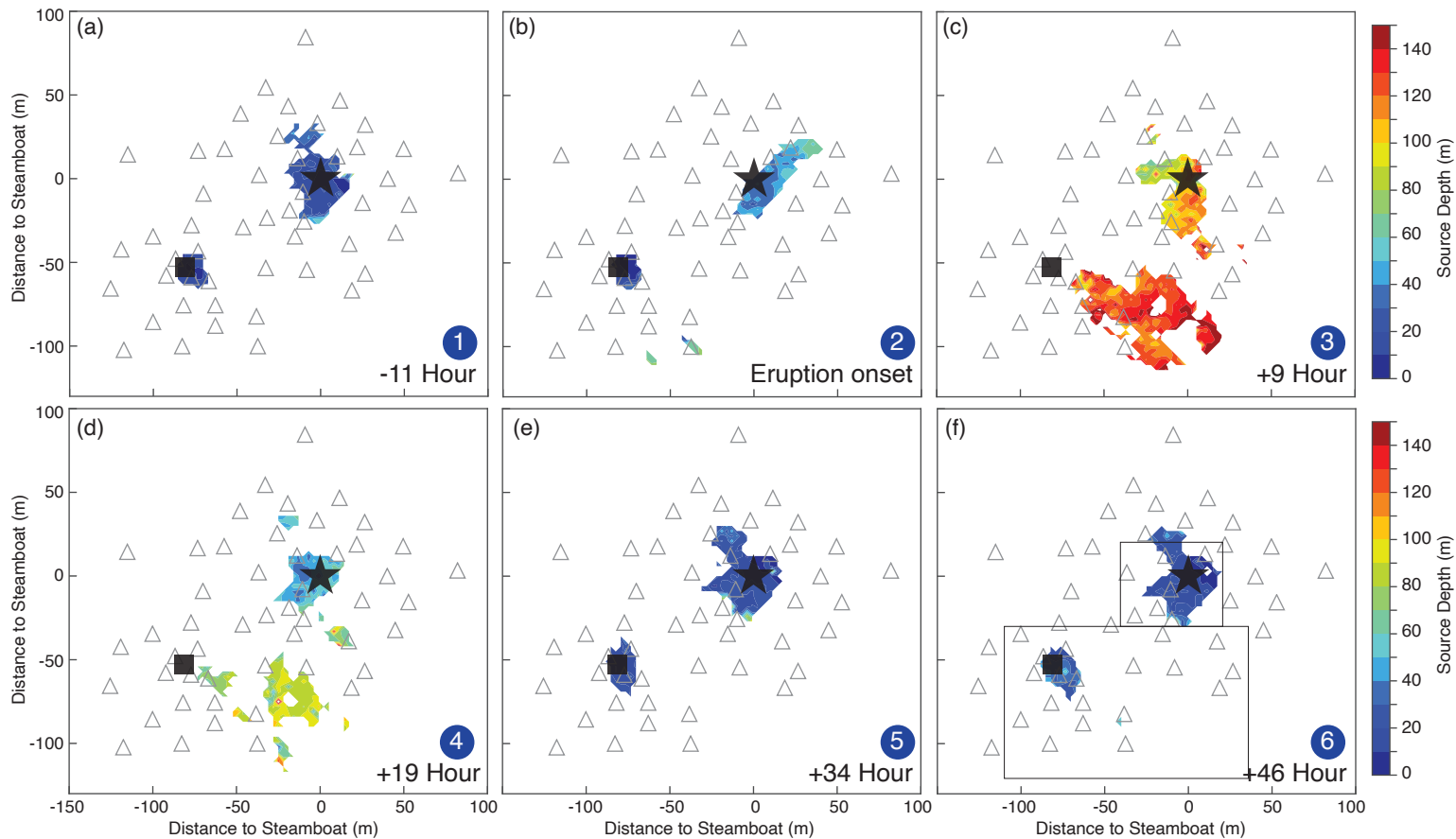**11 Hours before eruption**
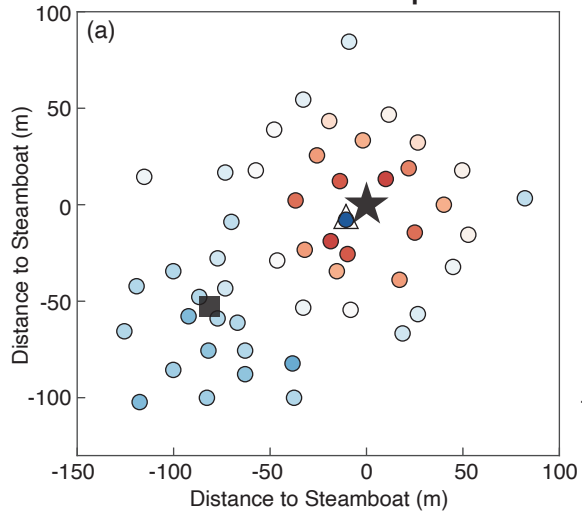
9 Hours after eruption
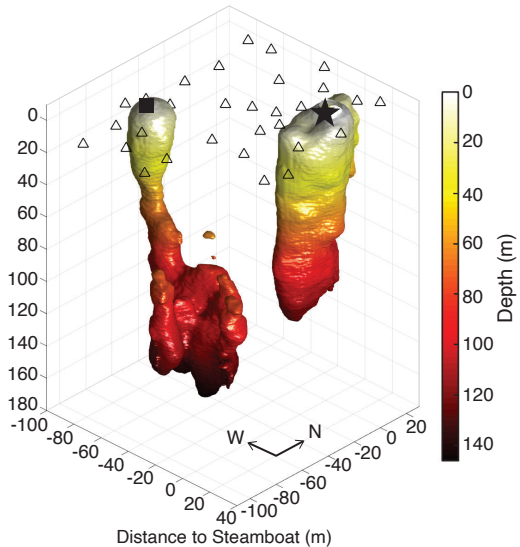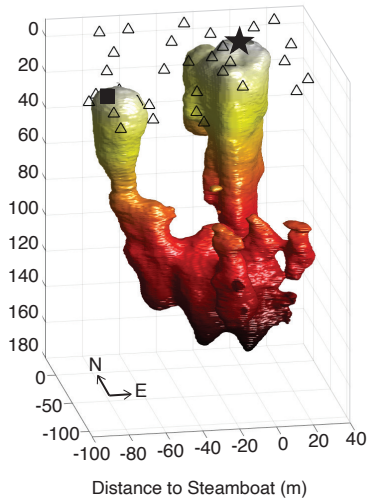
Figure7.

Figure8.

Depth (m)
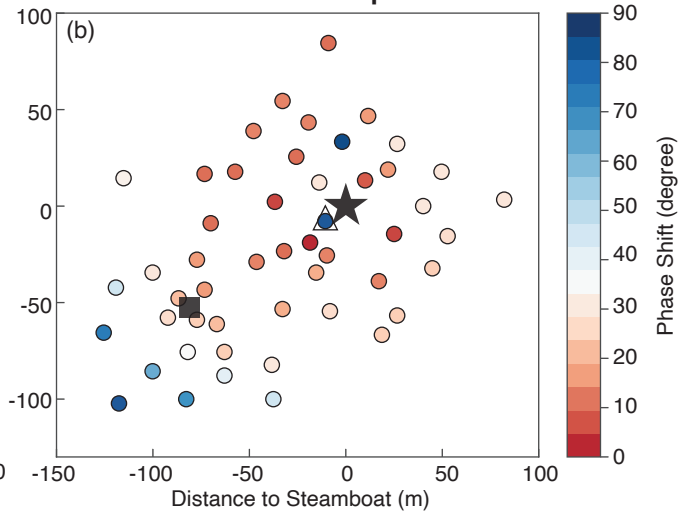
Figure9.

Recharge evolution

Source depth (m)

Date in 2019

Steamboat
Cistern

Figure10.

Figure11.

(a)

1 2 3 4 5 6

Source depth (m)

Start of minor eruptions

● Steamboat
● Cistern

(b)

Water depth (m)

Temperature (°C)

Water at Cistern refilled completely

No data

Start perturbance

Water below the transducer at 3.5 m

(c)

Amplitude (mV)

Steamboat Geyser

(d)

Amplitude (mV)

Cistern Spring

Hour relative to the eruption on July 11th 2019

Figure12.